Tectonophysics 717 (2017) 253–269

Contents lists available at ScienceDirect

Tectonophysics

journal homepage: www.elsevier.com/locate/tecto

3-D anatomy of an active fault-propagation fold: A multidisciplinary case study from Tsaishi, western Caucasus (Georgia)

A. Tibaldi [a], E. Russo [a,*], F.L. Bonali [a], V. Alania [b], A. Chabukiani [b], O. Enukidze [b], N. Tsereteli [b]

[a] University of Milan Bicocca, Department of Earth and Environmental Sciences, Milan, Italy
[b] M. Nodia Institute of Geophysics, M. Javakhishvili Tbilisi State University, Georgia

ARTICLE INFO

Article history:
Received 29 March 2017
Received in revised form 6 July 2017
Accepted 3 August 2017
Available online 09 August 2017

Keywords:
Active fold
Seismic hazard
Caucasus
Stress
Active fault

ABSTRACT

Ongoing deformation processes combining fault propagation and folding are the cause of diffuse seismicity in many areas of the world. A detailed understanding of the structural evolution of tectonically active folds is crucial for the evaluation of seismic hazard. This paper proposes an integrated analysis of an active fold, consisting in the development of a 3D model by combination of geomorphological observations, field geological-structural data and seismic reflection sections. Our case study is the Tsaishi anticline, located at the southwestern tip of the Rioni Basin uplifted area, at the foothill of Greater Caucasus (Western Georgia). We recognized that the fold started to form since the beginning of the middle Miocene, although preliminary data suggest the possibility of initial local uplift in the Oligocene. Folding process continues up to nowadays giving rise to a south-vergent anticline, as shown by upwarped late Quaternary river deposits. The fold backlimb is affected by three main backthrusts, whereas at the foot of the forelimb a main north-dipping thrust comes very close to the surface based on seismic sections. Here, field data show the presence of a 13-km-long fault scarp (or fold scarp). Along the scarp is located the epicenter of the strongest earthquake to date: the M_S 6.0 Tsaishi earthquake that struck the area in 1614 CE. Based on our results, we propose that the overall structure can be classified as an active fault-propagation fold. The recognition of its very recent growing associated with a major, underlying active fault, represents also a major contribution to the seismic hazard assessment of this populated area.

1. Introduction

Over the past decades, several attempts have been made at describing the processes controlling fold growth and evolution, with the help of two-dimensional geometric, analogue, kinematic and mechanical models (Suppe, 1983; Suppe and Medwedeff, 1990; Jamison, 1987; Fischer et al., 1992; Homza and Wallace, 1995; Wickham, 1995; Thorbjornsen and Dunne, 1997; Dubey, 1997; Costa and Vendeville, 2002; Cardozo et al., 2003; Mitra, 2003; Molinaro et al., 2005). These geometric models have encompassed the third dimension, through the development of 3D models of fault-related folds, obtained from the correlation among adjacent cross sections (Wilkerson et al., 1991; Fischer and Woodward, 1992; Shaw et al., 1994; Fischer and Wilkerson, 2000; Rowan and Linares, 2000; Wilkerson et al., 2002; Tanner et al., 2003; Zanchi et al., 2009). When dealing with tectonically active folds and the underlying active faults, which may be associated with strong earthquakes, one more concern arises, which is not limited anymore to the understanding of the structural evolution of the fold itself. The main goal at this point is to define and update the seismic hazard assessment of the area based on the evaluation of possible hidden faults (e.g. Fiorini and Tibaldi, 2012). In our study, we propose an integrated analysis consisting in the development of a 3D model, based on high quality, 2D seismic reflection sections and improved by the combination of new field geological, structural and geomorphological data. In fact, in our work, a multidisciplinary approach to the study of tectonically active folds is crucial for the development of a three-dimensional model aimed at the comprehension of the fold growth, evolution and recent tectonic activity. The use of seismic reflection sections to describe the lateral development of folds has been applied in the past, for example, by Apotria and Wilkerson (2002), in the Rosario structure, Maracaibo basin, Venezuela, or by Li et al. (2010), who produced a 3D structural model of the Longmen Shan fold-and-thrust belt (Sichuan province, China) by using seismic reflection sections, well data, geological observations and relocated aftershocks.

We chose the Tsaishi fold as a case study, a structure that is located along the southwestern margin of the Rioni Basin uplifted area (Fig. 1C), between the Greater and Lesser Caucasus, in western Georgia (Fig. 1A–B). This area is characterized by ongoing mountain building processes and is subject to diffuse compressional seismicity with magnitudes as great as 7 (Tsereteli et al., 2016). In particular, the M_S 6.0 1614 CE Tsaishi earthquake occurred just south of the anticline

* Corresponding author.
E-mail address: e.russo11@campus.unimib.it (E. Russo).

http://dx.doi.org/10.1016/j.tecto.2017.08.006
0040-1951/

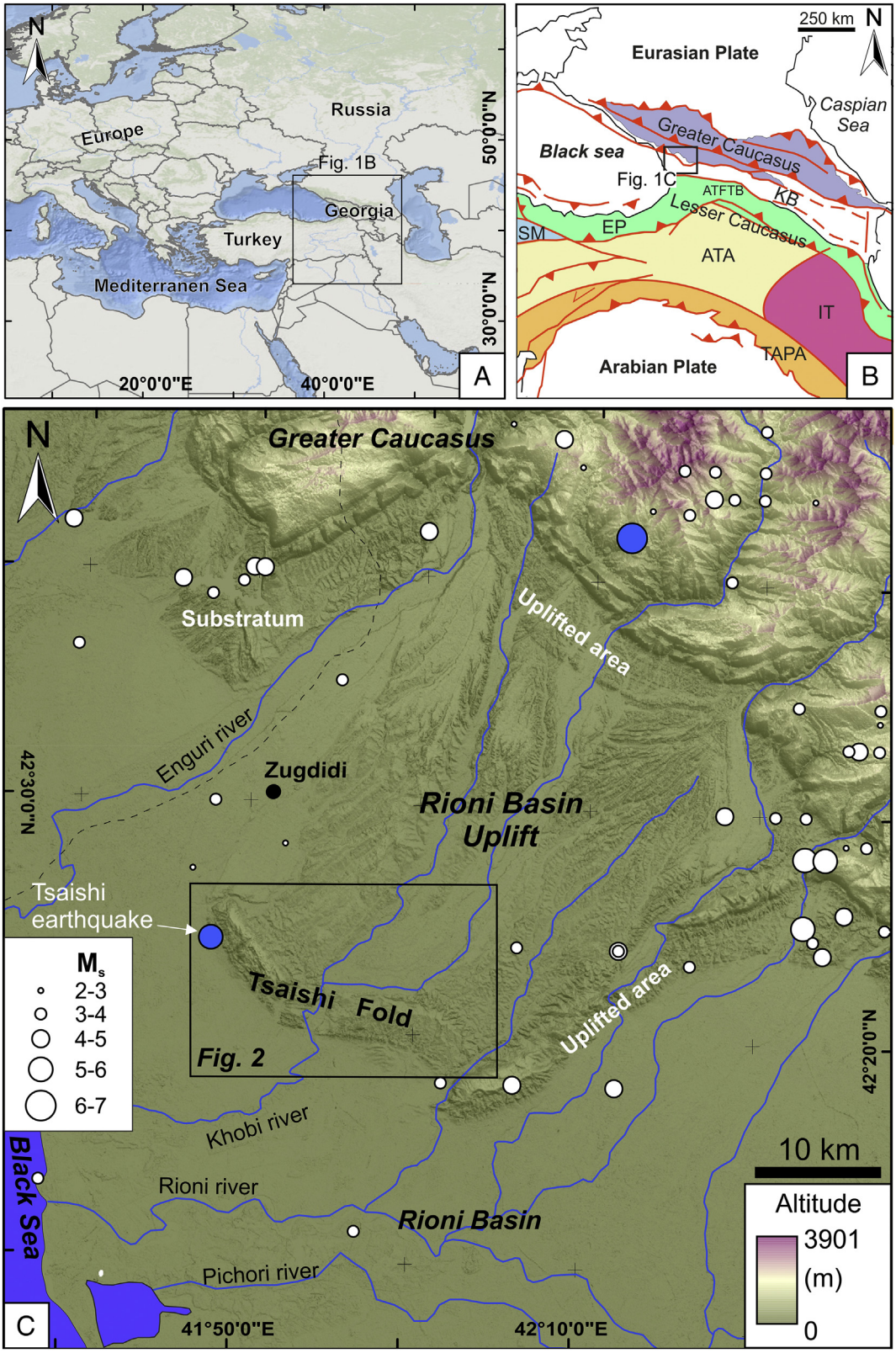

Fig. 1. A) Inset showing the location of Georgia and of Panel B. B) Tectonic map of the Arabia-Eurasia collision zone (modified from Sosson et al., 2010b). Abbreviations: ATFTB-Achara-Trialeti fold and thrust belt; KB-Kura Basin; EP-Eastern Pontides; ATA-Anatolide-Tauride-South Armenian Block; SM-Sakarya massif. C) Digital Elevation Model of the Rioni Basin uplift area (modified after Tibaldi et al., 2017); main rivers are shown. Seismicity is also reported, with white dots for post-1900 earthquakes (instrumental era, Zare et al., 2014) and blue dots for historical earthquakes (Varazanashvili et al., 2011), all scaled with magnitude. Location of Fig. 2 is also indicated. The 1614 CE Tsaishi earthquake is located (Varazanashvili et al., 2011). Apart from the Tsaishi fold, all the uplifted areas are indicated. The 30-m digital elevation model was provided by The Japan Aerospace Exploration Agency (JAXA - http://www.eorc.jaxa.jp/ALOS/en/aw3d30/; Takaku et al., 2014; Tadono et al., 2014). (For interpretation of the references to color in this figure legend, the reader is referred to the web version of this article.)

(Varazanashvili et al., 2011) (Fig. 1C). Our results enable distinguishing between multiple episodes of crustal deformation, and providing geometric and kinematic constrains as well as a possible explanation for the evolution of the Tsaishi fold and associated faults, which are key aspects for an improved seismic hazard assessment of the area. Our innovative approach has broad applications worldwide in any other region affected by compressional tectonics and fold growth.

2. Geological settings

2.1. The Rioni Basin

The Tertiary collision between the Arabian and Eurasian plates is at the origin of the formation of the Caucasus mountain system, a young orogen composed of two main ranges, the Greater Caucasus to the north and the Lesser Caucasus to the south (Fig. 1B). These two mountain belts are separated by the Transcaucasian intermontane depression, where the Rioni and Kura basins were formed as foreland basins during Oligocene-early Miocene times and were then involved into the orogenic fold and thrust belts (Adamia et al., 1977, 2010, 2011a, 2011b; Banks et al., 1997; Mosar et al., 2010; Sosson et al., 2010a, 2010b, 2013; Forte et al., 2010; Alania et al., 2016). Whereas the western Greater Caucasus has a single southward vergence, the central and eastern parts are composed by a double-vergent orogenic wedge (Forte et al., 2014).

Mountain building processes in the Caucasus are still active; in fact, recent GPS data show an eastward increase in the convergence rate between the Greater and the Lesser Caucasus, from 4 mm/yr in the Rioni basin to the west to 14 mm/yr in the Kura foreland to the east, consistently with the westward ongoing propagation of the closure of the Transcaucasian depression (Reilinger et al., 2006). The resulting, complex plate boundary interactions, are at the origin of vertical and horizontal strain partitioning in both the Greater and Lesser Caucasus (Rebai et al., 1993; Koçyiğit et al., 2001; Reilinger et al., 2006; Tan and Taymaz, 2006). In general, deformation and N-directed thrusting started earlier in the Lesser Caucasus than in the Greater Caucasus: palaeomagnetic rotations start in the Eocene for the Lesser Caucasus (Meijers et al., 2015), while significant active deformation 'hard collision' started only in the late Miocene for the Greater Caucasus (see Cowgill et al., 2016 and Rolland, 2017).

Furthermore, other indicators of still active tectonics are: *i*) a diffuse and high seismicity (Tsereteli et al., 2016); *ii*) magmatic activity, which started much earlier in the Lesser Caucasus (Eocene) than in the Greater Caucasus (late Miocene), along volcanoes located on both belts (e.g. Mount Elbrus, Greater Caucasus) (Rebai et al., 1993; Adamia et al., 1977, 2017; Koronovskii and Demia, 1999; Pasquarè et al., 2011; Sahakyan et al., 2016).

The Tsaishi anticline is located at the southwestern tip of the Rioni Basin uplifted area, between the southwestern Greater Caucasus and the northwestern part of Lesser Caucasus (Fig. 1B–C). The Rioni Basin developed in Oligocene-Miocene times through loading by the Achara-Trialeti fold-and-thrust belt, which represents here the northernmost front of the Lesser Caucasus, and the Greater Caucasus fold and thrust belts (Banks et al., 1997). The basin was filled by Tertiary sediments that rest above the substrate Mesozoic rocks, and have been subject to compressional (inversion) tectonics in Plio-Quaternary times. This is attested to by structural and geomorphological observations: locally uplifted, Cretaceous-Neogene marine and continental deposits, Plio-Quaternary river deposits located at heights of 200 m above the surrounding plane, the tilting of Quaternary strata and, last but not least, the presence of crustal seismic activity (Tibaldi et al., 2017). The infilling of the Rioni Basin is deformed with south-vergent asymmetrical folds at the margins of the uplifted area (some of which with a left-stepping en-echelon geometry), gentle symmetrical folds in the interior, and one main recent south-dipping reverse fault, corresponding to a backthrust (Tibaldi et al., 2017). Furthermore, Cowgill et al. (2016) showed distinct sedimentary sources on both sides of the Transcaucasus basin until the Late Miocene, which suggest a late closure (Late Miocene) for the Greater Caucasus Basin.

A thin-skinned tectonic style and en-échelon ramp anticlines of Cretaceous-Neogene strata dominate the northern part of Rioni foreland, formed in response to compression in the Greater Caucasus (Banks et al., 1997; Adamia et al., 2010, 2011b). These anticlines developed from the Middle Miocene onwards, mostly during the Meotian (Late Miocene – Sosson et al., 2010a), above south-vergent thrusts that detach and flatten along the Upper Jurassic evaporites of the Rioni foreland basin (Banks et al., 1997). The southern front of Rioni basin is composed of compressional ramp anticlines formed initially from the Early Sarmatian (12–10 Ma, Upper Miocene) to the Pontian (7–5 Ma, Upper Miocene) with minor growth continuing into the Quaternary (Banks et al., 1997; Adamia et al., 2010). The initial closure of the Rioni basin followed a major phase of uplifting, recorded to the southeast in the central Lesser Caucasus, where apatite fission-track data show exhumation at 18–12 Ma BP (Cavazza et al., 2015). This has been interpreted by the same authors as reactivation of a preexisting NW-SE-striking suture zone in the form of reverse dip-slip movements. In addition, uplift in the Lesser Caucasus started earlier than in the Greater Caucasus, probably in response to initiation of N-directed faulting related to closure of the Greater Caucasus Basin on its southern rim (see Cowgill et al., 2016; Rolland, 2017), as a result of a jump of subduction after the collision of Arabia with the Taurides-anatolia-SAB (as also suggested by Cavazza et al., 2015).

2.2. Stratigraphy of the Tsaishi fold area

The main stratigraphic units of the study area, ranging from Lower Cretaceous to Quaternary times, are shown in Fig. 2. In regard to the Tsaishi anticline, ages of outcrops are from the Lower Cretaceous to the Upper Miocene (Meotian). The oldest formation, exposed at the NW outcropping segment and corresponding to the Lower Cretaceous (Aptian and Albian, Cr_1 ap + al), is made of: *i*) claystones; *ii*) marls; *iii*) limestones; and *iv*) sandstones. Moving to the SE along the anticline, Upper Cretaceous deposits crop out, and are represented by two different units. The first and older one (Cenomanian age - Cr_2 cm), is composed of: *i*) sandstones; *ii*) claystones; and *iii*) limestones. The second and youngest one (Turonian-Danian Age - Cr_2 t-d), extending to very beginning of the Paleocene, is represented by: *i*) limestones and marls; *ii*) basaltic lavas, tuffs, tuff breccias; and *iii*) sandstones, claystones and limestones.

Moving progressively outward from the anticline core and top, ages become progressively younger, mainly belonging to the Tertiary (T - Paleogene and Neogene Periods), both along the N and NE flanks and the S and SW flanks, respectively the backlimb and forelimb of the anticline.

The following Paleocene-Eocene units are present along both the backlimb and forelimb. The older unit (Paleocene-Lower and Middle Eocene - $Pg_1 + Pg_2^{1+2}$) is represented by limestones. The younger unit (Upper Eocene - Pg_2^3) is represented by: *i*) marls; *ii*) basaltic lavas; *iii*) tuffs; *iv*) sandstones; *v*) breccias; and *vi*) claystones.

Also the units dating from the Oligocene to the beginning of the Miocene ($Pg_3 + N_1^1$), are present along both the backlimb and forelimb and represented by: *i*) gypsum-bearing claystones; *ii*) sandstones; and *iii*) marls. A younger unit from the Middle Miocene (N_1^2) is made of: *i*) claystones; *ii*) sandstones; *iii*) marls; and *iv*) limestones. Furthermore, such unit represents the easternmost termination of the fold. The next unit is of Sarmatian age (Upper-Middle Miocene - N_1s) and crops out along the NW backlimb facing to the NE and along the SE forelimb facing to the S. It is represented by: *i*) claystones; *ii*) conglomerates; and *iii*) limestones.

The next unit is of Meotian age (Upper Miocene - N_1m) and crops along the SE forelimb; it is characterized by: *i*) conglomerates; *ii*) sandstones; and *iii*) claystones. Such unit is also present in the Basin. The recentmost unit associated with the Tsaishi anticline dates back to the

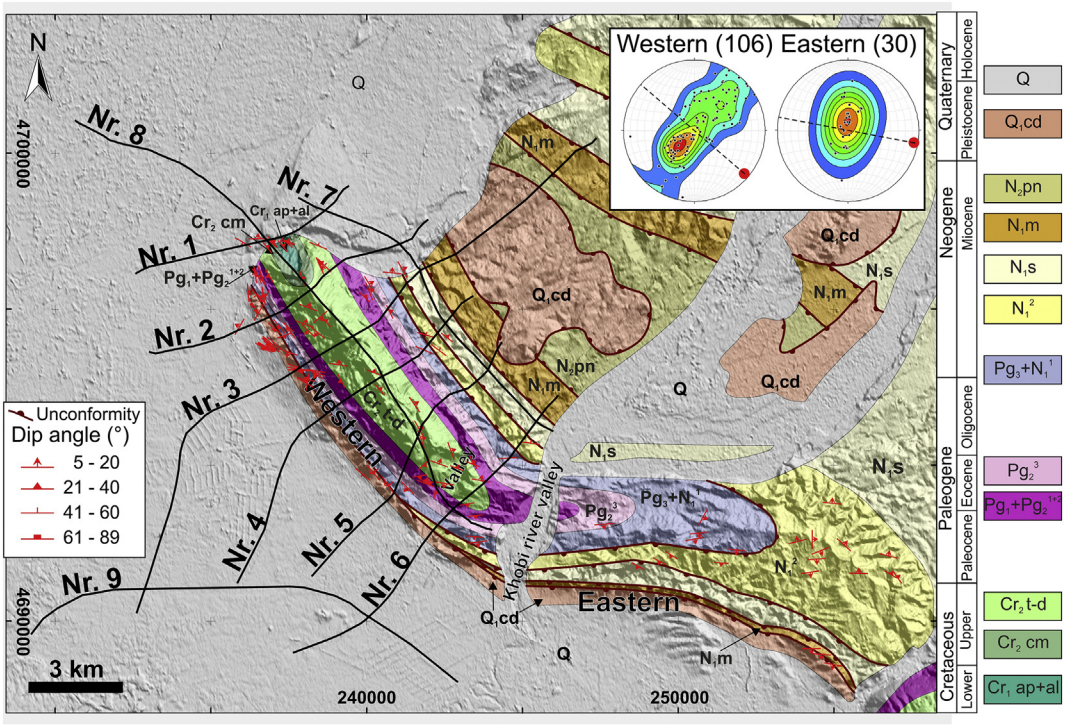

Fig. 2. Geological map of the Tsaishi anticline with field-measured strata attitude (modified after geological map of western Caucasus (K-38-XIII). 1956. Scale 1:200,000. Editor V. Kurochkin, compiled by A. Djanelidze and N. Kandelaki. Ministry of Geology and Mineral Protection USSR). Schmidt's stereogram, lower hemisphere, of strata attitude in correspondence of the western and eastern segment of the fold are shown; red dots represent the fold axis. Traces of seismic sections are also reported (black lines). Geological units: Q - Quaternary sediments; Q_1cd-Chaudian (Late Pleistocene) conglomerate and sandstone; N_2pn-Pontian (Upper Miocene) claystone, sandstone and conglomerate; N_1m-Meotian (Upper Miocene) conglomerate, sandstone and claystone; N_1s-Sarmatian (Middle Miocene) claystone, conglomerate and limestone; N_1^2-Middle Miocene claystone, sandstone, marl and limestone; $Pg_3 + N_1$1-Oligocene-beginning of Middle Miocene gypsum bearing claystone, sandstone and marl; Pg_2^3-Upper Eocene marl, basaltic lava, tuff, sandstone, breccias and claystone; $Pg_1 + Pg_2^{1+2}$-Paleocene-Lower and Middle Eocene limestone; Cr_2t-d-Turonian-Danian limestone, marl, basaltic lava, tuff, tuff-breccia, sandstone, claystone and limestone; Cr_2cm-Cenomanian sandstone, claystone and limestone; Cr_1ap + al-Aptian-Albian claystone, marl, limestone and sandstone. Geographic coordinates are shown in UTM-WGS84 projection. (For interpretation of the references to color in this figure legend, the reader is referred to the web version of this article.)

Late Pleistocene (Quaternary - Q_1cd); it crops out just on the entire forelimb and is represented by conglomerates and sandstones.

Other units crop out in the area and are mainly located north of the anticline, within the Rioni Basin. One is of Pontian age (Upper Miocene - N_2pn) and is represented by: *i*) claystones; *ii*) sandstones; and *iii*) conglomerates. A further unit is represented by Late Pleistocene (Q1cd - Chaudian layer) *i*) conglomerates; and *ii*) sandstones. The last one is Quaternary in age (Q - up to the Holocene) and is represented by undifferentiated sediments.

The presence of six unconformities among geological units has been recognized in the field (Fig. 2). Such unconformities are represented by: *i*) Late Pleistocene (Q_1cd) and Upper Miocene (N_2pn) units; *ii*) Upper Miocene (N_2pn and N_1m) units; *iii*) units of Oligocene-beginning of Miocene ($Pg_3 + N_1^1$) and Middle Miocene Epoch (N_1^2); *iv*) Middle Miocene (N_1^2) and Upper-Middle Miocene (N_1s) units; *v*) Upper-Middle Miocene (N_1s) and Upper Miocene (N_1m) units; and *vi*) Upper Miocene (N_1m) and Late Pleistocene (Q_1cd) units.

3. Methodology

To reconstruct the geological-structural architecture and geometry of the Tsaishi fold, we merged field surveys with other types of data. We used a digital elevation model (DEM) with a 30 m of vertical resolution, provided by the Japan Aerospace Exploration Agency (JAXA - Takaku et al., 2014; Tadono et al., 2014) as well as satellite images, with the purpose of: *i*) better defining the overall geometry of the anticline; *ii*) identifying morphological scarps and outcrops; *iii*) studying river flow and morphological anomalies. Seismic reflection sections and new field geomorphological, geological and structural data, have also been integrated.

Regarding field geomorphological data, we analyzed the possible presence of landforms that can represent the expression of prehistoric-historic near-surface faulting. These comprise scarps in the plain, tilted river terraces, and anomalous river diversions.

Geological-structural field data comprise measurements of strata attitude, wherever possible, aimed at better defining fold geometry at highest detail; microtectonic data have been collected in correspondence of all outcropping fault planes in order to define precisely their kinematics and their role in fold evolution; extensional joints and tectonic stylolites have been studied and used as complementary indicators of extension and horizontal compression, respectively. Special attention was paid to recognizing the succession of formation of these structures (e.g. Lanza et al., 2013). Slickenside fault planes have been separated in the field based on their age as resulting from crosscutting relationships among faults with different orientations. Slickensides of supposed similar age have been processed by way of the SG2PS software (Structural Geology to Post Script Converter - http://www.sg2ps.eu, by Sasvári and Baharev, 2014), with the purpose of reconstructing palaeostress tensors. Although this software enables performing palaeostress inversion through several methods, we used the INVD direct inversion method of Angelier (1990), because this methodology enables calculating a misfit vector "ν" between the measured and calculated shear vector, hence providing a chance to minimize the misfit.

Most importantly for our purpose, we compared and integrated results from field data with 9 seismic reflection sections provided by the State Agency for Regulation of Oil and Gas Resources of Georgia (SAROGR). Each of the seismic reflection sections was analyzed in detail, with the aim of identifying strata limits and faults and their geometric relations. A complete geological-structural key cross section based on

field data and time-migrated seismic reflection data has been prepared and tested by restoration.

Thanks to the interpolation between all the strata and tectonic structures identified in each section, integrated with our field data, we created a 3D model of the Tsaishi fold by means of the MOVE™ 2013 software (Midland Valley Exploration Ltd.), by joining faults and strata from each seismic section. First, we reproduced stratigraphic surfaces, then we reconstructed the faults.

Lastly, we compared and discussed the results derived from field data and the analysis of seismic sections, in order to define fold growth and evolution.

4. New field data

4.1. Strata attitude and fold geometry

According to DEM- and field-based geomorphological observations, the Tsaishi anticline has an outcropping total length of 29.4 km, taking into account that its NW part seems to be truncated (Fig. 2). Furthermore, the continuity of the outcropping part of the fold is interrupted by two narrow valleys trending NNE-SSW in its central portion (Fig. 2). In the next paragraphs we will consistently refer to the outcropping section of the fold, although it is possible that the fold originally stretched further to the NW.

The fold axis trends NW-SE in the western segment, whereas it trends E-W to WNW-ESE in the eastern segment. Along the western segment, which is 10 km long, we measured 106 strata attitudes (Fig. 2). Measurements belonging to the northern flank (backlimb – Nr. 39) have dip directions ranging N0–138° with an average value of N45°, with dip angles ranging 5–60° with an average value of 28°. Regarding the southern flank (forelimb – Nr. 67), we measured dip directions ranging N10°–300° with an average value of N193°, with dip angles from 5° to 89° and an average value of 46° (Figs. 2 and 3A). Furthermore, at two sites we locally surveyed overturned strata.

This results in an asymmetric anticline with a clear vergence to the SW and a NE-dipping axial surface, as shown in the Schmidt's stereogram in Fig. 2. By combining all measured strata attitude of the western part of the fold, we were able to precisely reconstruct the hinge line, which trends N147° in proximity of the NW part, and N125° along the SE part.

In correspondence of the eastern outcropping fold part, we measured strata attitude changes: Here they show dip directions mostly ranging N2°–345° (N70° as average value for 11 measurements) along the northern flank (backlimb), and N119–211° (N179° as average value for 19 measurements) along the southern flank (forelimb) (Fig. 2). Dip angle values range from 5° to 60° (24° as average value) and 8° to 60° (22° as average value) respectively (Fig. 2).

In proximity of the Khobi river valley the hinge line trends about E-W, while eastward there is another slight clockwise rotation of strata

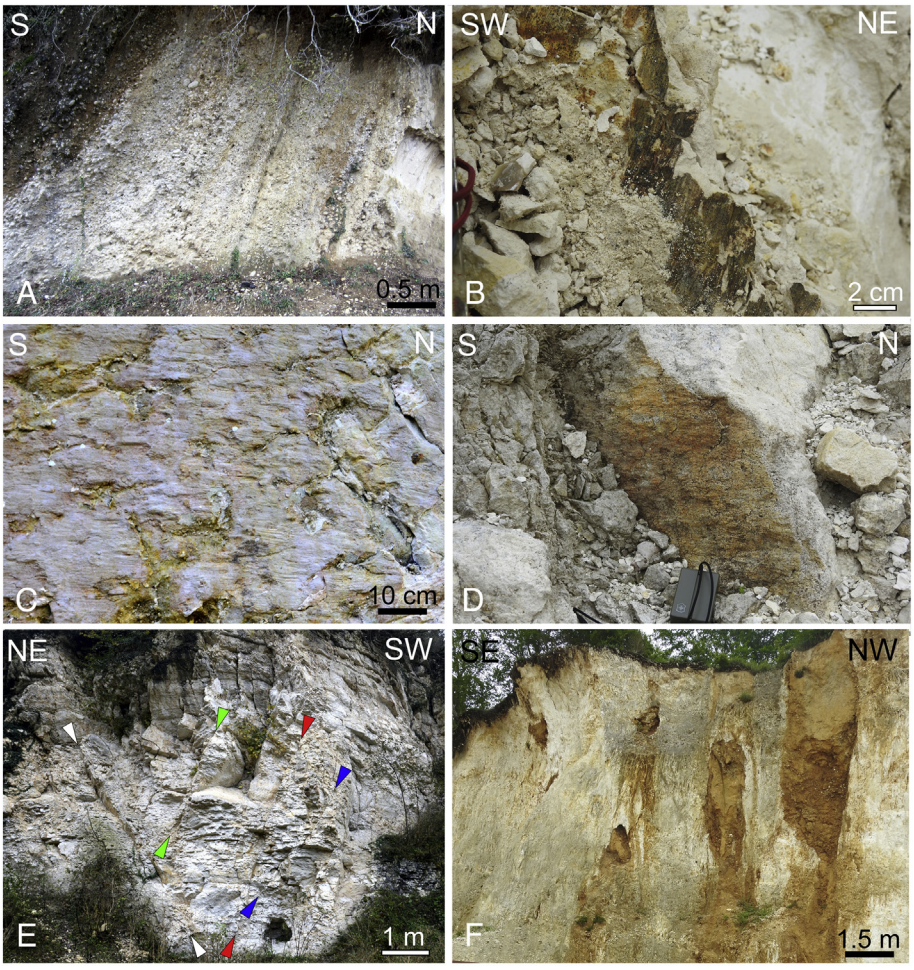

Fig. 3. (A) Steeply dipping strata, made of conglomerates of Late Miocene age, along the southern flank of the Tsaishi fold (42.395°N, 41.811°E). (B) Example of reverse fault plane with dip-slip striations (site 66a, Fig. 4). (C) Example of strike-slip fault plane with striations (site 167, Fig. 4). (D) Example of left-lateral strike-slip fault plane with crystal fibers and striations, compass for scale (site 67, Fig. 4). (E) Part of rock mass exposed at site 254, Fig. 4, with different fault sets. Each couple of triangles points to a main fault; the fault indicated by white triangles offsets the other faults. (F) NE-SW-striking extensional fracture, filled by brown karst deposits (site 66b, Fig. 4). (For interpretation of the references to color in this figure legend, the reader is referred to the web version of this article.)

up to N94° and further east the hinge line trends about WNW-ESE. Summing up the above, at the eastern part of the fold, from west to east, the hinge line trends N87°, N94° and N110° (Fig. 2).

4.2. Microstructural data

In order to better understand the evolution of the anticline, we collected new microtectonic data at all outcrops, which are entirely located at the western part of the Tsaishi fold, and then we integrated them with data previously collected by Tibaldi et al. (2017); results from this work are shown in Fig. 4 and Table 1. Particularly, the palaeostress tensor has been calculated at each site, providing plunge and dip for the greatest principal stress (σ_1) (Black converging arrows in Fig. 4), intermediate principal stress (σ_2) and least principal stress (σ_3) axis, the ratio (R (Φ)) between the differences of the principal stress eigenvalues, $(\sigma_2 - \sigma_3)/(\sigma_1 - \sigma_3)$, and the Misfit Angle (Av) expressed as the average angle between computed shear stress and slip vector. The orientation of the σ_1 has been assessed also based on the statistical trend of the peaks of tectonic stylolites. At some sites, we observed vertical fissures, from which we assessed the orientation of extension (diverging white arrows in Fig. 4). The trend of the σ_3 has also been measured based on the orientation of the growth of crystal fibers along veins. In all studied sites, fault offsets are of limited amount, from decimeters to meters. Locally, fault spacing is in the order of less than 1 m, indicating a penetrative brittle deformation. At some localities, preliminary studied by Tibaldi et al. (2017), reverse faults and strike-slip faults occur with a similar frequency. However, the outcrops we investigated show the predominance of strike-slip faults. Reverse faults have been found at sites 2, 66a and 249–253 (Fig. 4, e.g. in Fig. 3B), where they dip to the SSW, SE and NE, respectively. The calculated palaeostress tensors show horizontal σ_2 and σ_1, with σ_1 trending N13° at site 2, N118° at site 66a, and N42° at site 249–253.

Transcurrent faults are mostly of the right-lateral type along vertical to subvertical planes striking dominantly around NNW-SSE to N-S and about E-W (Fig. 4, e.g. in Fig. 3C–D). Subordinate vertical to subvertical, left-lateral strike-slip faults are also present, with dominant N-S to NE-SW strikes. The calculated palaeostress tensors show horizontal σ_3 and σ_1, with σ_1 trending mostly N6–52° (sites 67, 73, 159-160b, 167–170, 245, 254b), and subordinately N120° (e.g. site 159–160a).

The distinction of compressional phases has been possible for a few sites (e.g. Fig. 3E), showing that the about N6–52° trending σ_1 is more recent than the N120° trending σ_1; however, more field studies at other sites are needed to corroborate this result. The orientation of several horizontal stylolite peaks is consistent with a N5° direction of the σ_1 (sites 78 and 79).

At a few sites, the youngest structures are represented by small extensional fissures (e.g. Fig. 3F), which indicate a N130–140° extension, or a N40–50° σ_{Hmax} (sites 64, 66 and 66b-c). These have been found essentially along the southern flank of the Tsaishi fold, and we can rule out they were originated by gravity slope effects because: *i*) their strike is mostly parallel to the slope dip; and *ii*) they have been found in the interior of an open-air mine, far away from the nearest slope.

Summing up the above, we found different orientations of the σ_1 that tend to cluster at NNE-SSW, NE-SW and NW-SE. Extensional deformation also occurred along planes that are parallel to the NE-SW σ_1.

4.3. Geomorphological observations

By merging field geomorphological surveys, GPS detailed topographic profiles, and interpretation of satellite images, we were able to recognize a series of morphostructural features that contribute to shedding new light on the active structures of the Tsaishi area with Holocene activity.

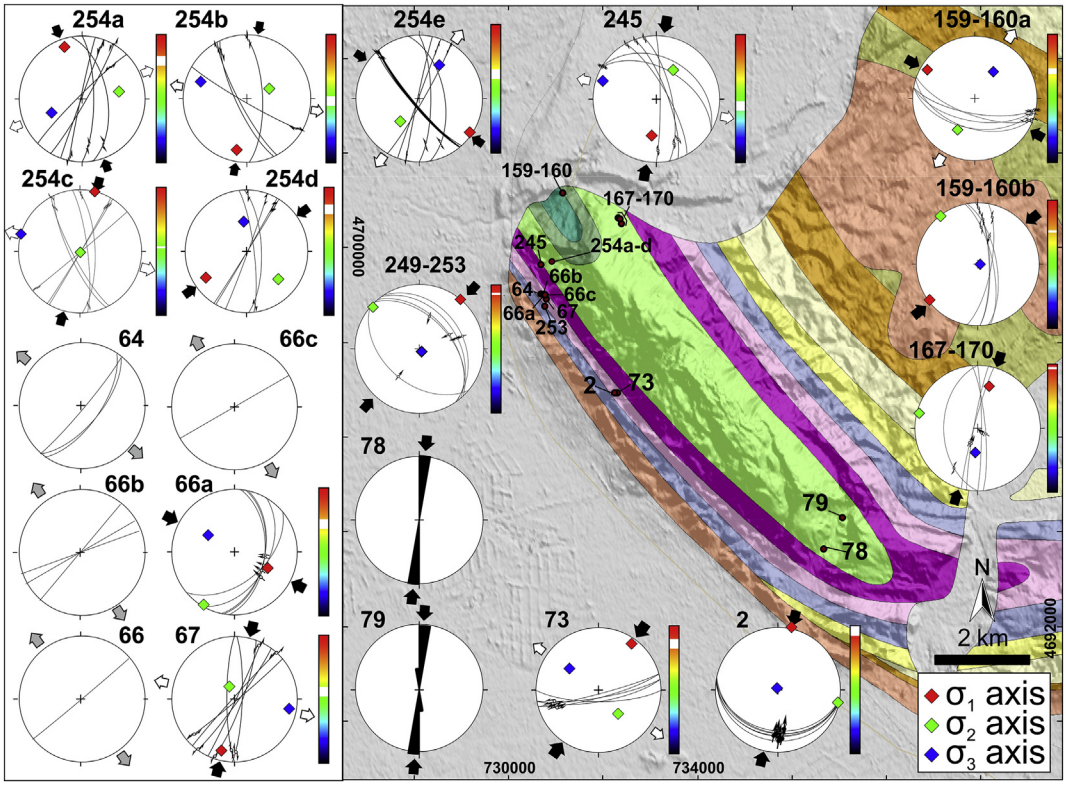

Fig. 4. Stereograms with results of palaeostress inversion at all outcrops of the Tsaishi fold. Slickenside fault stress inversion is expressed by converging black arrows for σ_1 and by diverging white arrows for σ_3. The orientation of the σ_1 has been assessed also based on the statistical trend of the peaks of tectonic stylolites (stops 78 and 79). At some sites, we observed the presence of small normal faults and vertical fissures, from which we assessed the orientation of extension (diverging light grey arrows). Geographic coordinates are shown in UTM-WGS84 projection.

Table 1
Results for palaeostress calculation. In table are reported: site number and location (Lat and Lon); number of data used during the inversion process; plunge and dip of resulting σ_1, σ_2 and σ_3; ratio (R (Φ)) between the differences of the principal stress eigenvalues, $(\sigma_2 - \sigma_3)/(\sigma_1 - \sigma_3)$; Av Misfit Angle = average angle between computed shear stress and slip vector; resulting tectonic regime. Some data are from Tibaldi et al. (2017).

Site	Lat (dd°)	Lon (dd°)	N. of data	σ_1 (plg/dip)	σ_2 (plg/dip)	σ_3 (plg/dip)	R (ϕ)	Av Misfit Angle	Tectonic regime
2	42.392	41.827	6	013/00	103/00	207/90	0.483	2.5	Pure compressive
66a	42.409	41.804	5	118/39	209/01	300/51	0.094	5.7	Transpressive
67	42.408	41.805	7	193/13	338/74	101/09	0.322	13.3	Pure strike slip
73	42.390	41.822	6	43/17	141/25	283/59	0.645	2.1	Pure compressive
254a	42.415	41.806	6	342/17	083/32	228/53	0.411	5.9	Pure compressive
254b	42.415	41.806	4	190/17	071/58	288/26	0.556	9.1	Pure strike slip
254c	42.415	41.806	7	015/03	155/86	285/03	0.404	13.8	Pure strike slip
254d	42.415	41.806	5	235/22	132/29	356/52	0.509	3.7	Pure compressive
254e	42.415	41.806	13	125/01	216/50	033/40	0.154	12.5	Transpressive
245	42.415	41.804	7	186/39	033/47	287/14	0.684	15.6	Pure strike slip
159–160a	42.428	41.810	6	300/15	204/22	061/63	0.131	2.4	Transpressive
159–160b	42.428	41.810	5	232/02	322/05	119/85	0.278	3.6	Pure compressive
167–170	42.422	41.825	5	017/34	283/07	183/56	0.903	15.6	Radial compressive
249–253	42,407	41,804	5	042/02	311/07	144/83	0.781	10.8	Radial compressive

At the foot of the southern flank of the Tsaishi fold, there is a series of uphill- and downhill-facing scarps. A detailed field survey allowed us to assess that these scarps coincide with the substrate strata attitude, and thus were produced as a consequence of morphoselection. In correspondence of the beginning of the plain at the foothill of the southern flank, a morphological scarp, facing SW, stands out and interrupts the continuity of horizontal surfaces (Fig. 5A). This scarp is quite continuous for several kilometers and does not coincide with any old or present river trace, and thus cannot be interpreted as a river terrace scarp.

Although locally it has been reworked for the construction of the railway, in most places the scarp shows a pristine morphology and clearly offsets the same horizontal topographic surface (Figs. 5A and 6A), as can be appreciated also by the detailed GPS topographic profiles that we surveyed in the field (e.g. Fig. 6C–F). Using these topographic profiles, we quantified the height of the scarp between about 3 m and a maximum of 7.5 m (Fig. 6A–C.). The area immediately north of the inferred scarp is affected by a series of small water streams characterized by entrenching due to intense erosion (e.g. Fig. 6B). The gully depth is in the order of 2–

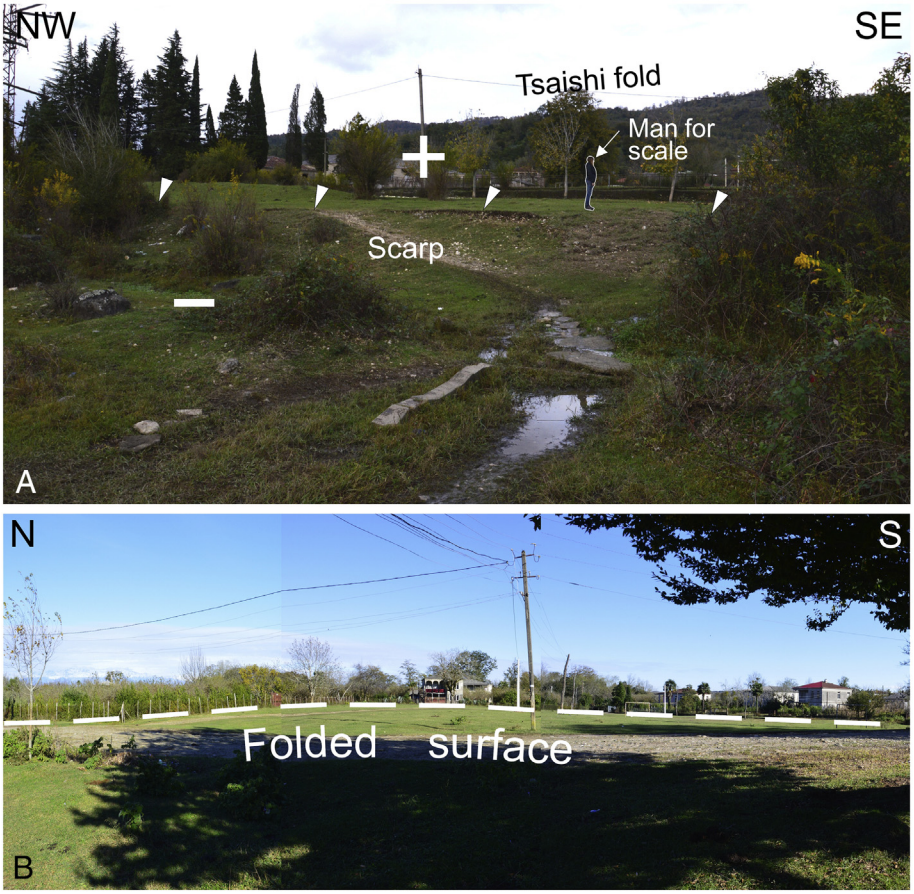

Fig. 5. (A) Photo of the SW scarp located at the southern foothill of the Tsaishi Fold (location in Fig. 6B). The white triangles point to the edge of the scarp that separates two offset horizontal surfaces. See man for scale. (B) Gentle upwarping of a Holocene river terrace in proximity of the northwestern termination of the Tsaishi Fold. The dashed white line indicates the curved topography.

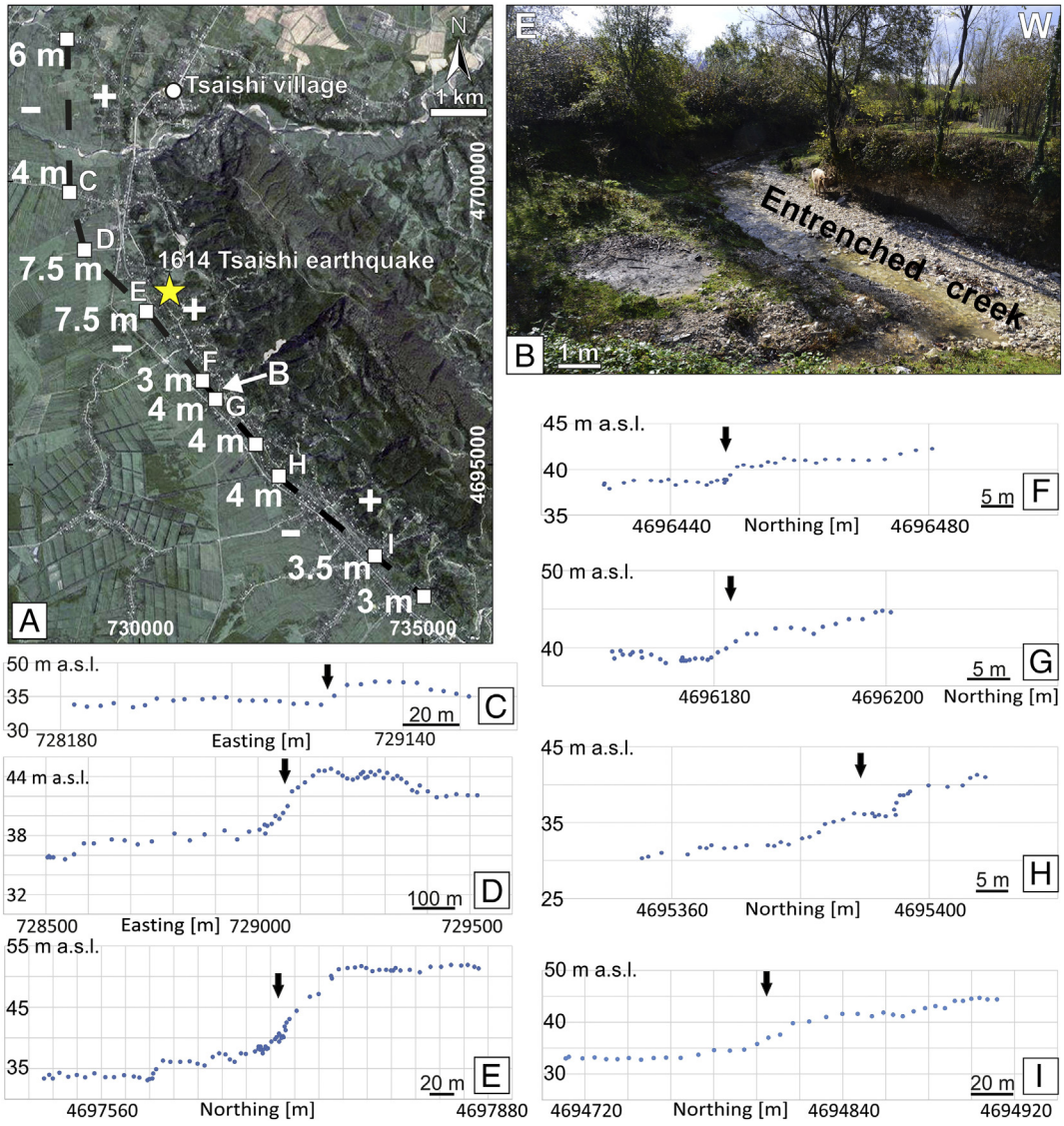

Fig. 6. (A) Trace of the inferred faults by GPS profiles and field surveys. Field and GPS-measured vertical offsets are reported as well as the location of the 1614 CE Tsaishi earthquake (yellow star). (B) Example of river stream deeply entrenched immediately north of the fault scarp, i.e. in the hangingwall block. (C–I) Topographic profiles across the fault scarps found at the foothills of the southern flank of the Tsaishi fold. Each section is located by the letter in Fig. 6A. (For interpretation of the references to color in this figure legend, the reader is referred to the web version of this article.)

3 m with respect to the surrounding flat topography. Once the creeks have flowed through the scarp, they suddenly change their morphology to a meandering pattern without any erosive processes. The described features are consistent with recent uplift of the area north of the scarp.

In regard to the Tsaishi fold, this shows some deeply-incised gullies, up to some tens of m deep, that suddenly become less incised at half of present fold limbs, suggesting complex river erosion during fold growth, similar to the observations made on an active fold in central Otago (New Zealand) by Jackson et al. (1996) (Fig. 7A). They represent the effect of strong water erosion that cannot be reconciled with the present position of the gully. The gullies formed when the fold was much less developed and then, as the fold developed, they became isolated. The rivers located now in the plain surrounding the fold, show instead clear diversions as they approach the fold (red river segments in Fig. 7B), whose growth acted as an obstacle to their southward flow. Only in two cases the rivers were capable of maintaining their course in correspondence of the two already mentioned NNE-SSW valleys crossing the fold (blue river segments in Fig. 7B). It is worth noting that these valleys are located exactly in correspondence of the abrupt change of attitude of the folded strata (e.g. Fig. 2).

In correspondence of the northwestern termination of the Tsaishi fold, there is a series of river terraces of Holocene age, elongated NNE-SSW (see Fig. 6 in Tibaldi et al., 2017). The surfaces of these terraces show a very shallow dip southward, consistent with the direction of river flow. However, approaching the Tsaishi fold, south of the town of Zugdidi, the dip of the uppermost (i.e. the locally older) terrace surface is northward; some outcrops also show the presence of beds of unconsolidated river conglomerates that dip 7–8° to the north (Fig. 8A–B). Both evidences indicate an uphill tilting of the river deposits. In correspondence of the northwest prolongation of the Tsaishi hinge line, the topography (and thus the river terrace) makes a culmination, whereas more to the south it attains once again a gentle dip to the south, consistent with the general river flow direction (Fig. 8C–D). As a whole, the topographic surface of this river terrace makes an anticline, which can be appreciated also in Fig. 5B.

5. Seismic sections analysis

The interpretation of nine seismic reflection sections, trending NW-SE (2), NE-SW (6) and E-W (1), provides a good coverage of the western

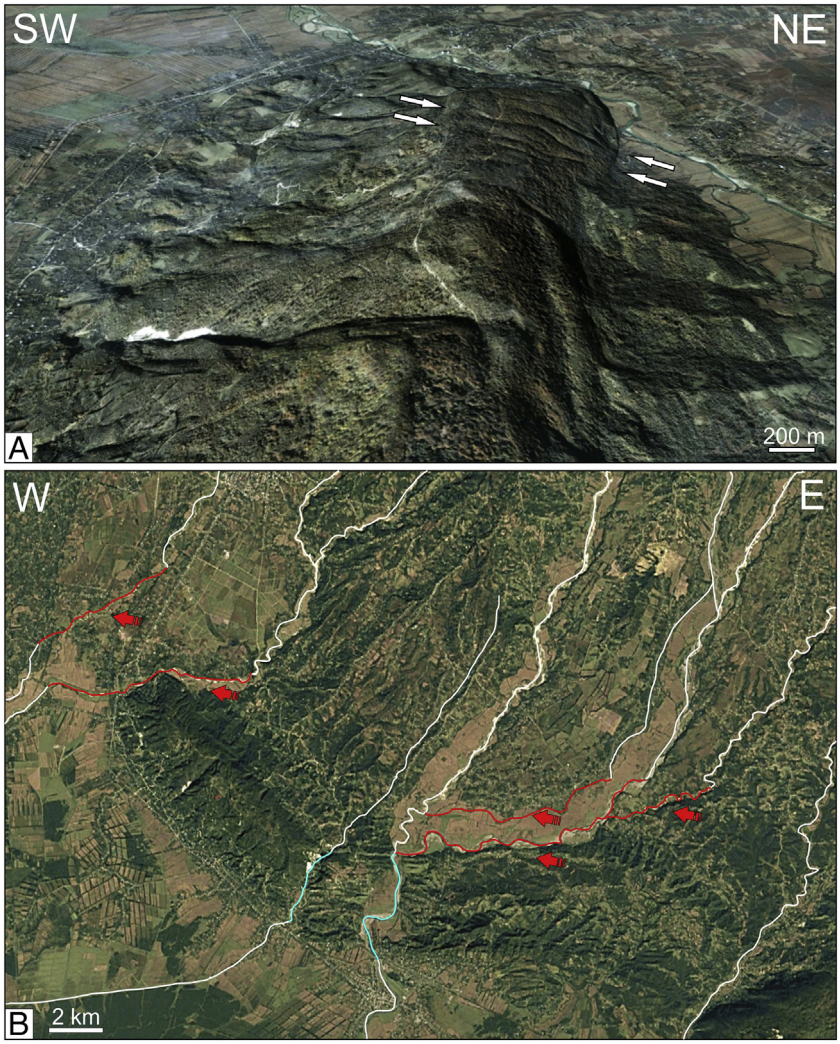

Fig. 7. (A) Oblique Google Earth view of the Tsaishi fold, showing examples of deeply-incised gullies that affect only parts of the fold (arrows). (B) Satellite image of the Tsaishi fold with indication of rivers normally flowing towards the SSW (white lines), which become diverted as they approach the fold (red lines); arrows provide the direction of diversion. The river segments in pale blue indicate the only two cases of rivers crossing the fold. (For interpretation of the references to color in this figure legend, the reader is referred to the web version of this article.)

part of the Tsaishi anticline (Fig. 2). The most significant seismic sections, that best describe the main features of the fold, are shown in Figs. 9 and 10. Fig. 11 shows the balanced geological-structural interpretation, consistently with field data, of the most significant seismic reflection section across the fold that has been time-migrated and checked by retrodeformation. The amount of shortening obtained from this part of the balanced cross-section is 43% (12 km). Horizontal displacement along Tsaishi fault-propagation fold is 1960 m. In addition, a complete 3D model based on all sections cutting the hinge line is shown in Fig. 12.

The uppermost parts of all the six NE-SW trending sections clearly show the presence of the south-vergent Tsaishi anticline, of south-vergent thrusts (F1, F2, F3; Fig. 9B–D–F) and of north-vergent backthrusts (B1, B2, B3; Fig. 9B–D–F), all of which involving strata of Cretaceous and Tertiary age (Fig. 9A–F for sections 1–2–3 located in Fig. 2).

The presence of the thrust F1 is confirmed by well data (location is shown in Fig. 9A and B): according to the combination of wells data and seismic sections, we are able to locate the fault F1 at a depth of 2700 m in correspondence of Well 3 and 3800 m at Well 4 (referred to topographic surface).

The Mesozoic succession (Cretaceous and Jurassic units) is made of parallel strata, whereas the uppermost parts of the seismic sections show more complex stratigraphic geometries. Along the southern fold flank (forelimb), there are unconformities between the Tertiary strata (e.g. Figs. 9B and 11); in particular, two main unconformities are given by the upper strata (1 Quaternary, 2 Upper Miocene-Meotis-Pontian, 3 Upper Miocene Sarmatian, 4 Middle Miocene) onlapping the lower strata (5 Oligocene-Lower Miocene), an indication of formation of the fold forelimb since the beginning of the middle Miocene. The recentmost main strata recognizable in the seismic sections (white line) forms an angle of about 10° to the lower strata. In turn, the topographic surface (black line) also makes an angle (of a few degrees) to the shallowest strata. Along the fold backlimb (i.e. to the north), the Tertiary strata thicken northward; this is evident for strata 5 to 1 (Oligocene-Lower Miocene (Maikopian) to Quaternary), whereas the strata 6 (Upper Eocene) and older are parallel each other with constant thickness (Fig. 11). This indicates a synsedimentary fold growth of the northern fold limb starting in the Oligocene.

F2 and F3 form a fan of low-angle reverse faults that splay from the main structure F1 (Fig. 9B–D–F). The latter is the main reverse fault that shows an about 620-m offset of Tertiary strata. In section view, thrust F1 is steeper than F2 and F3, and has a slight curved trace with an upward convex side.

The lower part of these NE-SW seismic reflection sections is characterized by an upper and lower detachment (UD and LD in Fig. 9B–D–F), which are located along decollement strata of Upper and Lower Jurassic

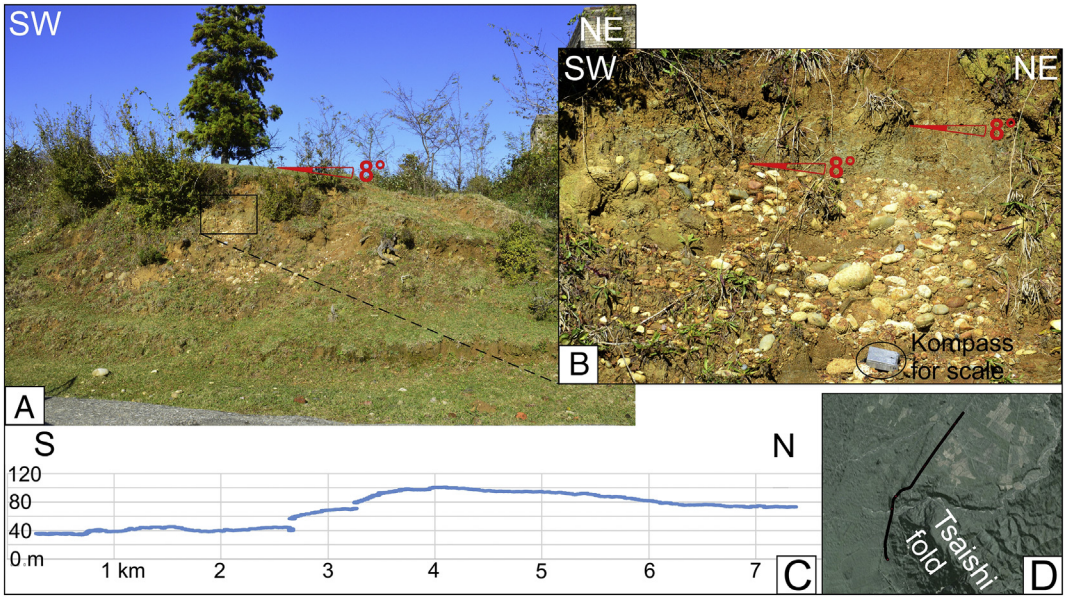

Fig. 8. (A–B) Photo of river deposits, belonging to the same terrace as in Panel A, tilted northward; location is provided by the red dot in Panel D. (C) Topographic profiles along the river terraces located at the northwestern termination of the Tsaishi fold. Note that the terrace has been upwarped to form a gentle anticline. The inset shows the GPS track (D). (For interpretation of the references to color in this figure legend, the reader is referred to the web version of this article.)

age, respectively. These two thrusts link with each other to the SW: among those, a series of south-vergent reverse faults are present, giving rise to a duplex structure, involving Middle-Lower Jurassic strata (e.g. Fig. 9B–D–F). The upper detachment links to the main south-vergent thrust F1 to the southwest in all the seismic reflection sections, giving rise to a split-apart structure.

The NW-SE striking seismic section 7 (Fig. 2 for location) is parallel to the Tsaishi fold axis and is located in correspondence of its backlimb (Fig. 10A–B). It is characterized by tilting of the Cretaceous strata to the NW, at the northwestern termination of the fold, whereas the along-strike dip of the strata flattens out to the southeast. Seismic section 8, still NW-SE trending, is located in correspondence of the Tsaishi fold axis. It shows the presence of an east-dipping reverse fault reaching the surface immediately northwest of the fold (Fig. 10C). The E-W striking seismic section 9 is located south of the Tsaishi fold and thus does not appear to have been affected by faulting and folding, being characterized by apparent horizontal to sub-horizontal strata in this along strike view (Fig. 10D–E).

6. 3D model analysis

The identification of south-vergent thrusts, north-vergent backthrusts and detachment surfaces in most of the seismic reflection sections allowed us to create a three-dimensional model of the Tsaishi anticline western segment, by using the MOVE™ 2013 (Midland Valley Exploration Ltd.) software; our goal has been to reconstruct its structure and thus understand its temporal and spatial evolution (Fig. 12). The 3D model shows a gentle dip of the strata along the Tsaishi fold backlimb with a sub-horizontal attitude, while the forelimb to the SW is characterized by a steeper attitude of the strata that terminate against the main NE-dipping thrust fault (F1). Thrust F1 has a dip that ranges from 30 to 40°. Dip angles of F2 and F3 are 20–30° and 5–20° respectively, all steeper to the northwest. The dip azimuth values of F1, F2 and F3 are 45–70°, 40–85° and 50–90° respectively.

The three north-vergent backthrusts (B1, B2 and B3) are visible along the backlimb of the Tsaishi fold: according to the 3D model, B1 has a steeper attitude to the northwest, where it reaches a dip of 75°, and it is less inclined to the southeast, where its dip ranges between 45 and 60°. The dip values of backthrusts B2 and B3 are more homogeneous, ranging from 40 to 55° and from 35 to 55° respectively, along their whole length. The dip azimuth of B1, B2 and B3 is 210–235°, 210–245° and 205–235°, respectively.

7. Discussion

7.1. Overall structure of the Tsaishi fold

The integration of data coming from field surveys, satellite images, digital elevation models, and seismic reflection sections, enabled obtaining a coherent, thorough picture of the overall geometry and geology of the fold as well as its structural architecture, and the individuation of the geometry and kinematics of the youngest structures, also useful for seismic hazard assessment.

The attitude of all outcropping strata indicates the presence of an asymmetric anticline with the axial surface dipping towards the NE at the western outcropping fold segment, and towards the N to the NNE along its eastern segment. Based on new field data, we observed that the northwesternmost part of the fold still has a cylindrical geometry, suggesting that originally the fold did not terminate here. Further northwest, the fold has been eroded, consistently with the high erosion rate of rivers in the area (e.g. Vezzoli et al., 2014). The present outcropping western segment of the fold represents the fold core where the oldest unit outcrops (Figs. 1–2).

The outcropping strata are quite continuous, being interrupted locally by faults with small offsets, in the order of cm to some m. These structures are mostly represented by strike-slip faults and subordinately by backthrusts dipping towards S to SW (Fig. 4). The main strata offsets occur in the hidden part of the fold, where seismic reflection sections clearly indicate a series of main reverse faults (e.g. Fig. 9). The southern fold flank is offset by three, shallow-dipping reverse faults (Fig. 11, F1, F2 and F3 in Fig. 12), which, as a whole, create a footwall shortcut thrust fan. Seismic sections also indicate that the strata of the southern fold flank stop against the uppermost fault of the thrust fan (F1), which has the major offset. The strata here dip around 50–60°, which is consistent with field data showing a gradual steepening of the fold strata southward. The opposite northern flank of the fold, with strata dipping 20–50°, is offset by three steeper reverse faults (B1, B2 and B3 in Fig. 12), giving rise to an imbricate fan of forward-breaking backthrusts. In the footwall of the lowest of these backthrusts, the layers attain a gentler dip and finally become sub-horizontal northward. The general

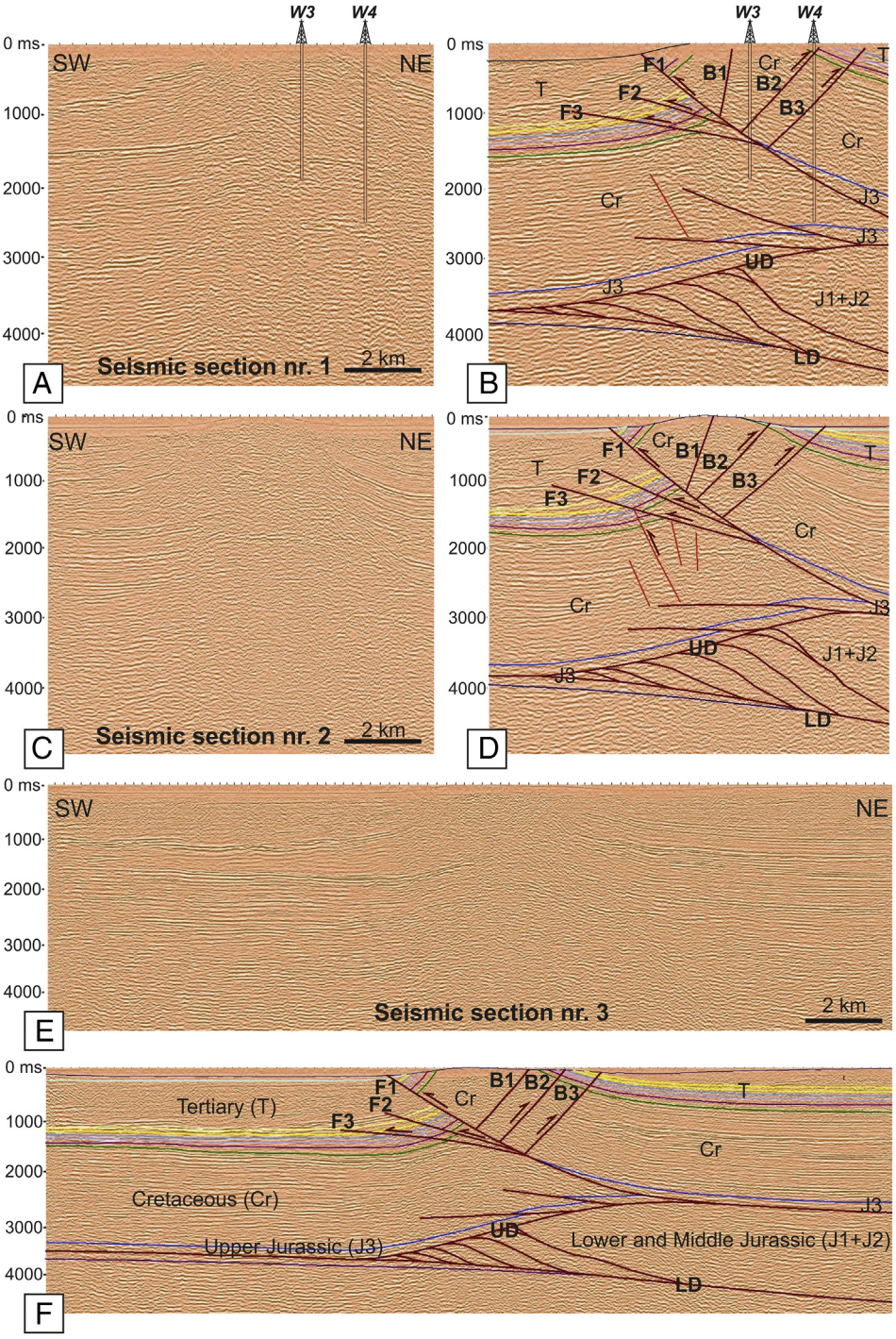

Fig. 9. Uninterpreted and interpreted time-migrated seismic reflection sections number 1 (A–B), 2 (C–D) and 3 (E–F). Location of seismic sections is in Fig. 2. F1, F2 and F3: south-vergent thrust faults. B1, B2 and B3: north-vergent backthrusts. UD and LD: upper and lower detachments. J1 + 2: Lower and Middle Jurassic; J3: Upper Jurassic; Cr: Cretaceous; T: Tertiary. Fault kinematics for the uppermost part shown. Well 3 (W3) and Well 4 (W4) are located in sections number 1 (Panels A–B).

geometry of the Tsaishi anticline is thus a fault-propagation fold, consistent with the model of Suppe and Medwedeff (1990), complicated by frontal thrust and backthrust fans.

In general, fault-propagation folds show at the base a low-angle propagating ramp that progressively loses slip. The ramp usually terminates upwards at a blind tip, where shortening is attained by a buckle syncline fold (Williams and Chapman, 1983; Suppe and Medwedeff, 1990; Mitra, 1990; Pace and Calamita, 2015). As the shortening increases, the forelimb and the syncline are offset by breakthrough thrusting; this results in an asymmetric fold with a steeply-dipping to overturned forelimb and a gently-dipping backlimb. In our case, the frontal upper breakthrough thrust (F1) has completely cut the rock succession, reaching up to the surface.

Below the basal thrust of the Tsaishi fold, there is another series of thrusts, represented by a duplex structure that contributes to create a split-apart system just in correspondence of the position of the Tsaishi fold (Figs. 11 and 12). This suggests that the strong uplift of this area may have been also determined by the thickening at depth of the rock succession in correspondence of the split-apart structure.

The change in the fold hinge line orientation between the western and eastern segments of the Tsaishi fold occurs in correspondence of two river valleys (Fig. 2), which might hide minor faults. The similarity

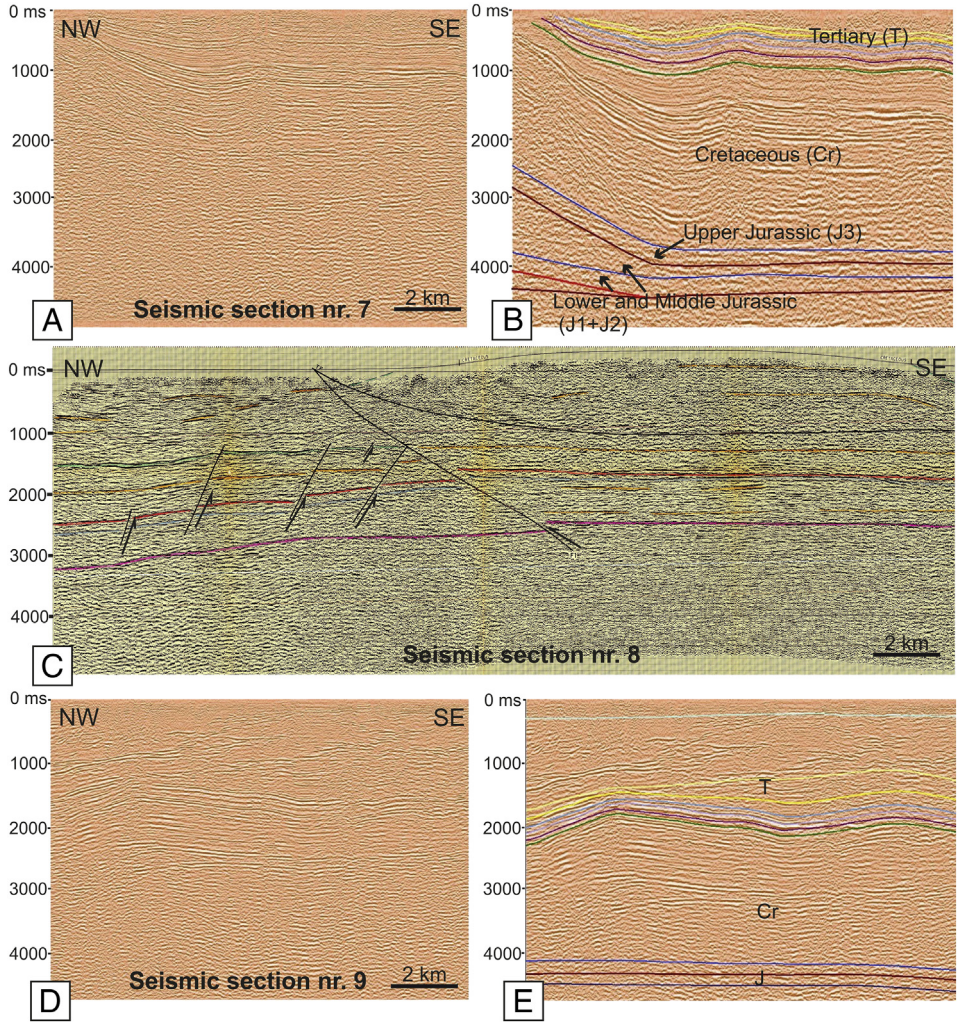

Fig. 10. Uninterpreted and interpreted time-migrated seismic reflection sections number 7 (A–B), 8 (C) and 9 (D–E). Location of seismic sections is in Fig. 2. F1, F2 and F3: south-vergent thrust faults. B1, B2 and B3: north-vergent backthrusts. UD and LD: upper and lower detachments. J1 + 2: Lower and Middle Jurassic; J3: Upper Jurassic; Cr: Cretaceous; T: Tertiary.

of the general shape of the two segments suggests that they may represent a continuous structure, represented by a 29.4 km-long anticline with a curved hinge line in plan view. It is plausible that the entire structure is a fault-propagation fold.

The very close contact between the eastern termination of the Tsaishi fold with another fold, located immediately to the southeast (Fig. 1), suggests the possible presence of a hidden reverse fault that offsets the interposed tight syncline.

The higher dip angle of the imbricate fan of forward-breaking backthrusts offsetting the Tsaishi backlimb and their lower offset amount with respect to the thrusts of the forelimb, together with the slight upward convex profile of the uppermost frontal thrust, suggest that the south-dipping backthrusts were produced by the adaptation of the hanging-wall block during its ramping along the steeper part of the forelimb thrust. This implies that the backthrusts developed later during the fault-propagation fold evolution.

The geometry of the strata evidenced in the seismic reflection sections, shows thinning of strata or onlap structures in correspondence of the Tsaishi fold that start in the Oligocene and beginning of the middle Miocene (Fig. 11). This is in part older than the compression from the middle Miocene onwards indicated by Sosson et al. (2010a) for the anticlines of the northern part of Rioni Basin, or from the early Sarmatian (beginning of Upper Miocene) (Banks et al., 1997; Adamia et al., 2010). Anyway, compressional phases of early-middle Miocene have been individuated by Cavazza et al. (2015) in the central Lesser Caucasus with major uplifting at 18–12 Ma BP that should correspond to the initial closure of the southern rim of the Rioni Basin, and several pre-middle Miocene compressional events were recognized by Saintot and Angelier (2002) in the Greater Caucasus west of the area here studied. We thus suggest the possibility that some initial uplift/folding process started at Tsaishi before the main compressional events of middle-late Miocene, although more detailed studies are necessary to constrain this earlier phase.

7.2. Fault and fold kinematics

The kinematics analysis of the various parts of the Tsaishi fold, resulting from stress inversion of outcropping slickenside fault planes, shows very complex movements. Different stress tensors correspond to contractional and extensional deformations. Compression is given by σ_1 parallel and perpendicular to the fold hinge. The presence of different stress tensors at the same site clearly indicates that the rock mass underwent different deformations associated with events of different age. We will discuss first the compression perpendicular to the Tsaishi fold axis and then the compression parallel to fold axis.

The NNE-SSW to NE-SW compression directions are generally consistent with the development of the fold, although the orientation of the σ_1 is not always parallel to the shortening directions as computed by the strata dips and related fold geometry. In particular, the whole western outcropping segment of the Tsaishi fold has a geometry

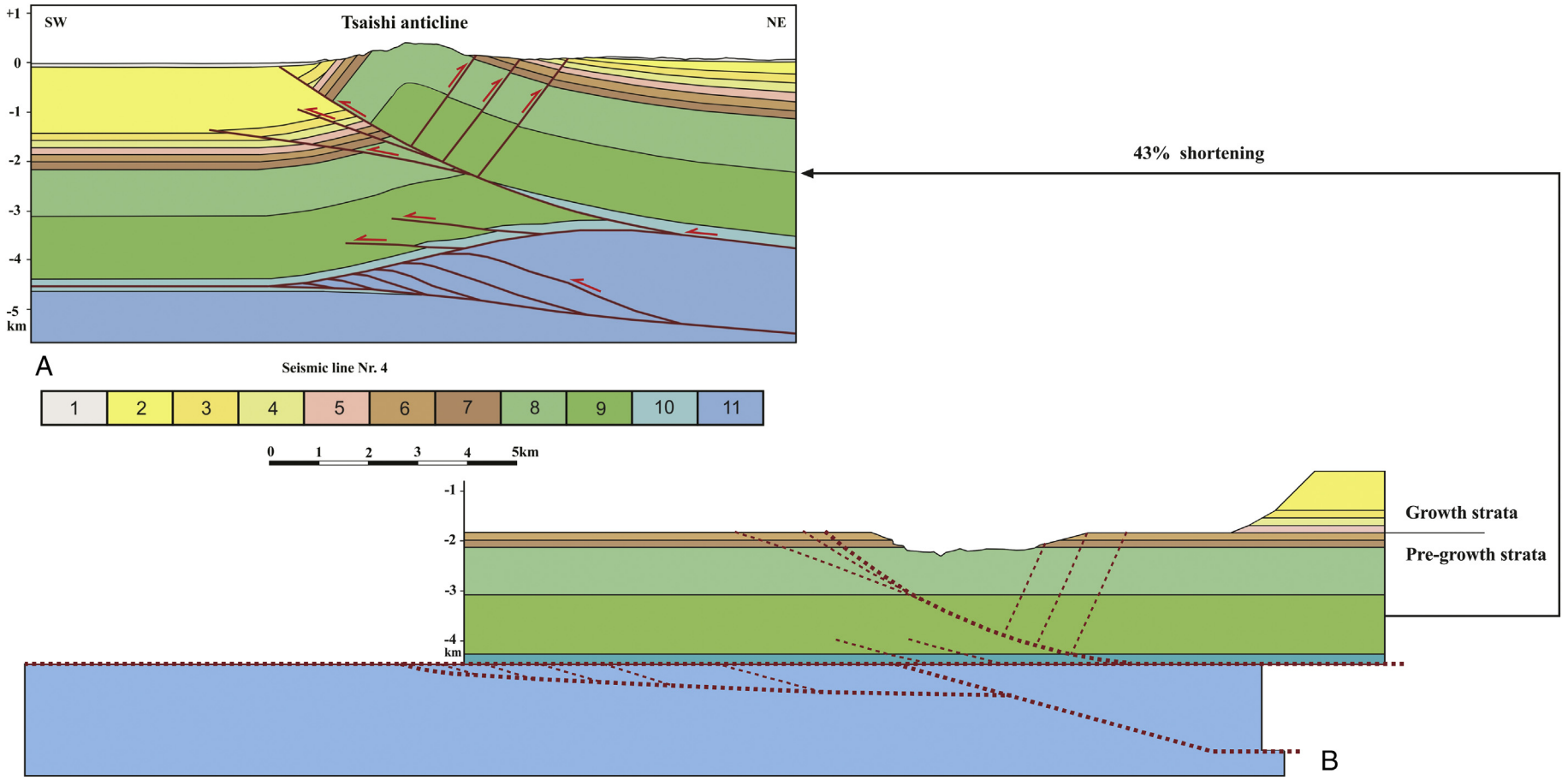

Fig. 11. (A) Geological cross-section across Tsaishi anticline, based on the interpretation of time-migrated seismic section Nr. 4 (location in Fig. 2) and field data. 1-Quaternary; 2-Upper Miocene (Meotis-Pontian); 3-Upper Miocene (Sarmatian); 4-Middle Miocene; 5-Oligocene-Lower Miocene (Maikopian); 6-Upper Eocene; 7-Middle Eocene; 8-Upper Cretaceous; 9-Lower Cretaceous; 10-Upper Jurassic; 11-Lower-Middle Jurassic. (B) Restoration of the geological cross-section.

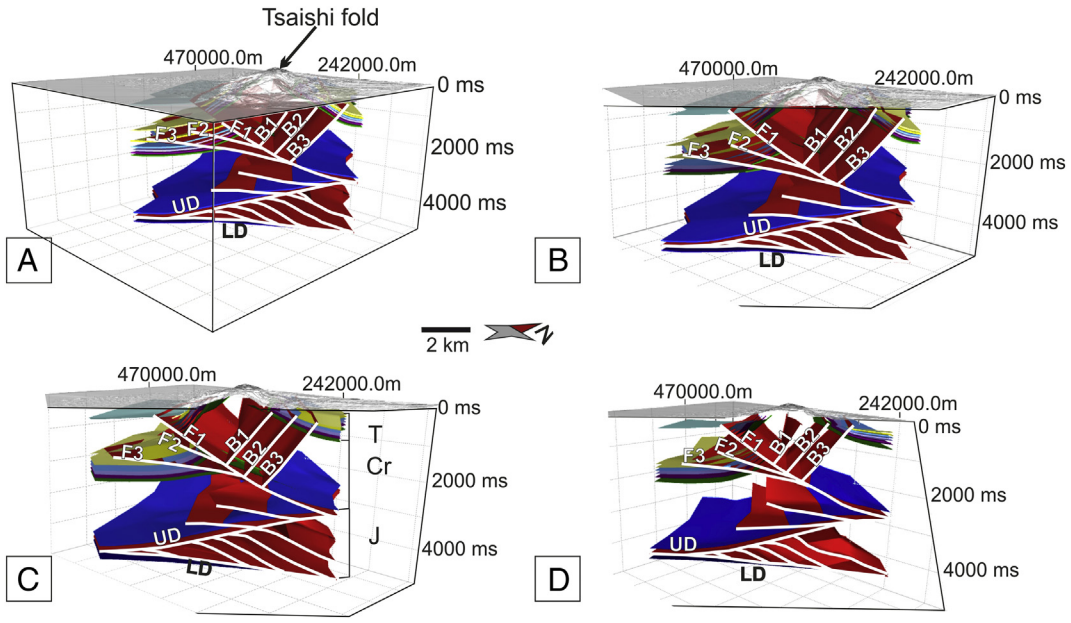

Fig. 12. 3D reconstruction of the faults and folds in the Tsaishi area based on seismic reflection sections and field data. F1, F2 and F3: south-vergent thrust faults. B1, B2 and B3: north-vergent backthrusts. UD and LD: upper and lower detachments. Geographic coordinates are shown in UTM WGS84 projection.

compatible with a N45° main direction of shortening (Fig. 2). The main reverse fault F1, which accompanied the development of the fold, has dip azimuth between N50–70°. We can thus conclude that the NE-SW compression direction computed by the slickenside fault planes is compatible with these data. Nevertheless, the NE-SW direction of σ_1 recorded by faulting is not consistent with the recentmost stress field based on focal mechanism solutions (Tsereteli et al., 2016), as shown for two focal mechanisms in Fig. 13, and thus may represent clockwise rotation of the fold (Fig. 13A–B).

The measured NNE-SSW trending σ_1 at the Tsaishi outcropping faults is instead oblique respect to the shortening direction of the western fold segment. This direction is fully consistent with the regional Quaternary stress field and thus may represent the latest record of brittle deformation of the studied rock masses (Fig. 13B). This suggestion is also consistent with field data that show that the strike-slip faults generated by the NNE-SSW trending σ_1 offset the faults linked with the NE-SW trending σ_1.

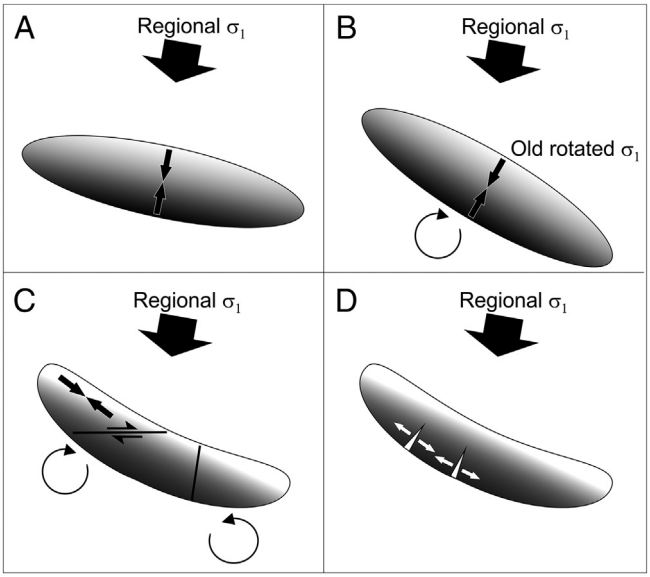

Fig. 13. Sketch with a tentative reconstruction of the evolution of the Tsaishi fold. (A) Indicates the first fold formation, which was accompanied by small-offset faults consistent with a NNE-SSW trending σ_1. (B) Mechanism of fold clockwise rotation that may explain the presence of structures that correspond to a NE-SW directed σ_1. (C) Bending of the fold along a vertical axis and development of compression parallel to the fold hinge. (D) Late development of extension parallel to the fold hinge at the forelimb.

Shortening took place both by reverse and strike-slip faulting. Reverse faulting appears to be the oldest deformation phase, also due to the presence of several reverse planes that show steeper dip, which is compatible with post-faulting tilting. Strike-slip faulting is much more diffuse and most planes are vertical and offset the reverse faults; these data indicate that strike-slip faulting developed later in the fold evolution. However, all these structures have small offsets denoting that they represent small-scale brittle deformation in response to pervasive shortening during folding.

A more complex scenario is related to the presence of the NW-SE direction of σ_1, which corresponds to shortening parallel to the fold hinge. This is by no means compatible either with the Quaternary regional state of stress, or with the regional Neogene deformation field. The NW-SE shortening occurred mostly as a consequence of strike-slip motions, here interpreted as small scale disruption of the original fold by block faulting in consequence of the clockwise rotation of the fold along a vertical axis (Fig. 13C). This rotation is consistent with the final curvature of the whole outcropping fold in plan view. It might also be that local NW-SE compression developed in response to the collision with the other fold located immediately southeast of the Tsaishi fold (for further details see Dzhanelidze and Kandelaki, 1956). A further explanation for the compression parallel to the fold hinge may be linked to the proximity of the western segment of the Tsaishi fold with a possible lateral ramp. In fact, if we assume that the main reverse fault F1 (Fig. 12) represents the frontal ramp of the compressional system, the NNE-SSW fault already hypothesized northwest of the Tsaishi fold by Tsereteli et al. (2016) and Tibaldi et al. (2017) should be a lateral ramp with oblique to transcurrent motions. Following the model of Apotria (1995), at the leading intersection zone of a frontal ramp with a lateral ramp, which is convex towards the transport direction of the hanging-wall block, displacement paths converge in the hanging-wall, giving rise to lateral shortening. This can result in contraction parallel or sub-parallel to the axis of a fold located above the ramp intersection. Finally, it must be cited that Saintot and Angelier (2002) show the presence of WNW-ESE oblique contraction during the early Miocene in

western Greater Caucasus. They suggest that this compression parallel to the orogenic belt resulted from the convergence between the Arabian Plate and the Caucasian system.

At some sites, it has also been possible to detect extensional fractures. These structures seem to be the youngest among all brittle discontinuities, and this suggests that they developed during the late stage of the folding process. The extension direction is parallel to the western outcropping fold hinge line but has been found essentially along the forelimb (i.e. the southern flank). This localized hinge-parallel extension may result from two possible mechanisms: *i*) stretching that develops during incremental folding at the external, convex side of the fold limb in consequence of its arcuate geometry (Fig. 13D); and/or *ii*) an increase in the vertical stress in consequence of an upward-directed push exerted by the thickening of the duplex or of the split-apart system below the fold, with consequent rotation of the σ_1 that attained a vertical position.

By considering also the structures detected by seismic reflection, we can conclude that the Tsaishi fold developed during four main stages: *i*) initial folding of the strata and cutoff of the forelimb, accompanied by pervasive small-scale reverse and strike-slip faulting; *ii*) propagation of backthrusts across the fold backlimb; *iii*) bending along a vertical axis of the fold with the hinge line attaining a general curved shape in plan view, accompanied by local shortening parallel to the hinge line; and *iv*) extension in the forelimb parallel to the fold hinge, and NNE-SSW compression dominating at the backlimb. Nevertheless, we need to underscore that this reconstruction of a succession of processes may be improved by further studies; in fact, such reconstruction is difficult due to the inherent complexity of the area and the limited number of good outcrop exposures.

7.3. Active structures

Based on the seismic section data, the main reverse fault F1 (Figs. 11 and 12) comes very close to the surface at the foothills of the southern and western sides of the western segment of the Tsaishi fold. Anyway, it is necessary to admit that seismic reflection resolution does not allow appreciating if the fault really reaches the topographic surface. Here, field data show the presence of a series of NW-SE to WNW-ESE trending morphostructural scarps that may be explained as the surface expression of Holocene faulting (Figs. 6 and 14) or active folding (e.g. Chen et al., 2007), due to the lack of fault exposure. Further research through trench excavations is required for a better understanding of the origin of these scarps. These morphostructures are represented by scarps facing towards the southwest; there is no other possible explanation, either in terms of river erosion or in terms of anthropic causes. River erosion is not a possible explanation for these scarps because they are perpendicular to the general direction towards SSW of the river flow. An anthropic origin must also be ruled out because the observed features are too long to be imputable to cultivated terraces or similar. Only locally, the construction of the railway may have changed the original landforms. The scarps are mostly parallel to the fold hinge line and crop out in correspondence of the upward prolongation of the frontal thrust F1 detected by seismic reflection. Since these scarps face southwest, this is also compatible with uplift of the hanging-wall block, i.e. with reverse kinematics.

The location, geometry and kinematics of thrust F1 is also compatible with the other topographic anomalies that we detected further to the north. Immediately northwest of the Tsaishi fold, in fact, the northward tilting of the topographic surface is compatible with an ongoing process of ramping of the fold over the upward-concave frontal thrust. This topographic surface attains an upward-convex shape near the western termination of the Tsaishi fold, compatible with an ongoing anticline folding process (Fig. 14). At a few outcrops it has been possible to notice that these topographic surfaces coincide with the upper surface of Holocene alluvial deposits, that are thus folded.

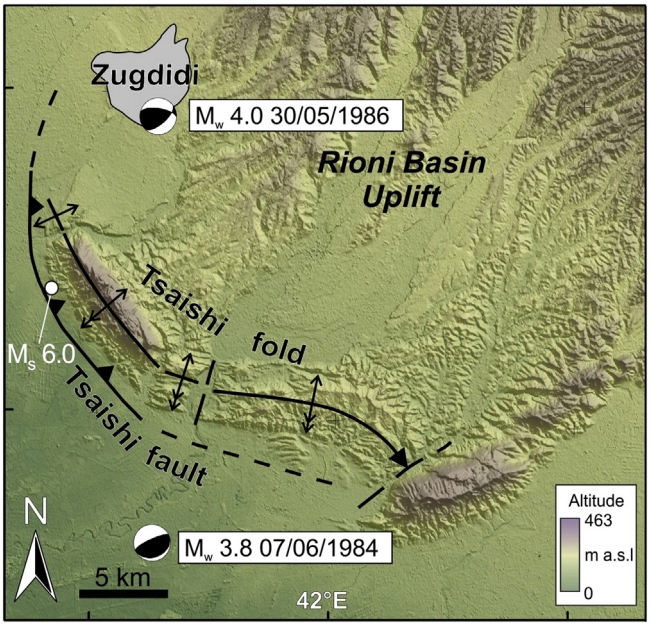

Fig. 14. Main active structures of the southern part of the Rioni Basin uplifting area. The hinge line of the Tsaishi fold is indicated, together with the Tsaishi reverse fault running southwest of the fold. The fold is interrupted by an east-dipping reverse fault coinciding with the fault detected on the seismic reflection section. Dashed line where fault is inferred. Focal mechanisms relative to the area are shown (from Tibaldi et al., 2017).

We conclude that all the above observations are evidence of an active reverse fault capable of deforming the topography for a total surface length of 13 km at minimum, here termed "Tsaishi fault". The surface deformation may be the direct expression of the fault slip plane that cut all the strata, or may be a fold scarp involving the surface strata. This zone of shallow deformation coincides exactly with the location of the historic Tsaishi earthquake of 1614 CE (Fig. 6; Varazanashvili et al., 2011). The same authors assigned an Intensity to the epicenter of $I_o = 8–9$. Although the intensity points are few, the chronicles of that time indicate that the Tsaishi church and many buildings of the same village collapsed, and also several other villages were destroyed (Dadiani, 1962). Zakaraia (1956), in particular, reconstructed that "The earthquake shocks of great strength that lasted for the whole year (1614) destroyed not only the Tsaishi ensemble but also the nearest churches and villages as well". The M_S 6.0 assigned by Varazanashvili et al. (2011) corresponds to the possibility of faulting along a plane capable of reaching the surface. Although the length of the scarp that we found in the field may be consistent with the structure that moved during this latest major M_s 6 earthquake, the height of the scarp is up to 7.5 m, suggesting that it did not develop entirely during this latest seismic event (e.g. Wells and Coppersmith, 1994; Blaser et al., 2010). Such scarp should represent the final product of successive incremental fault motions, possibly encompassing a long time interval. Recent (late Holocene) uplifting of the hanging-wall block, i.e. of the block located northeast of the scarp, is also consistent with the presence of erosive river gullies on this block, whose over-incision terminates in correspondence of the scarp.

These data indicate the presence of recent folding and shallow reverse faulting, both with vergence to the south. Folding and faulting are thus compatible with each other, and can be reconciled in terms of a still ongoing process of formation of the Tsaishi fault-propagation fold. This process is consistent with the Plio-Quaternary inversion tectonics of the Rioni Basin that is expressed by a series of shortening structures with southward vergence (Tibaldi et al., 2017) and widespread seismic activity (Tsereteli et al., 2016). At present, the area along the southern foothills of the Tsaishi fold is inhabited with hundreds of small scattered houses and those located in the village of Khobi, built without applying any anti-seismic criteria. The town of Zugdidi,

counting about 43,000 inhabitants (latest census in 2012), is located 10 km away from the possible active fault plane emersion. By considering that the Tsaishi fault (F1 in Fig. 12) dips to the NE and that the location of the 1614 Tsaishi earthquake is estimated, it is possible that the location of earthquake epicenter, both for past and future times, may be more to the North, even closer to Zugdidi, with a deeper hypocenter. The presence of all these settlements, together with the described structural framework, suggest to take into consideration this area as being subject to seismic hazard and risk.

8. Conclusions

Part of the Rioni Basin, located at the foothill of the Greater Caucasus, is punctuated by a series of morphological highs that are jutting out of the plain. The southwesternmost topographic high is made of Cretaceous-Tertiary rocks that have been uplifted and folded to create the Tsaishi anticline. The field data that we collected allowed us to reconstruct the shallow structure of this fold and recognize the presence of indicators of still active uplifting, faulting and folding processes. We integrated these data with seismic reflection sections in order to reconstruct the general geometry and evolution of this structure.

The outcropping Tsaishi anticline is made of two segments trending NW to the west and E-W to the east. The northern flank of the fold (backlimb) is characterized by strata dip angles up to 60°, whereas the forelimb is made of steeper strata to the SW. These steep beds extend downward until they stop against a main reverse fault dipping to the NE. This fault belongs to a fan of reverse low-angle thrusts imaged by the seismic sections. They cut through a tight syncline and then gradually fade out southward; the uppermost fault, instead, points to the surface. Exactly in correspondence of the possible emersion of this fault, we found field morphological evidence of a scarp striking NW-SE. This scarp may represent the surface fault rupture trace of an active main reverse fault, here named Tsaishi fault, or may represent a fold scarp linked with the very shallow reverse fault. The location of the scarp and the related fault geometry are compatible with the historic M_s 6.0 Tsaishi earthquake that happened in 1614 CE, which attests to the seismic hazard of the area.

The backlimb strata maintain their gentle dip downward where seismic sections indicate they gradually attain a horizontal attitude. The fold backlimb is offset by three main backthrusts. The overall geometry of the Tsaishi fold is thus given by a fold-propagation fold limited at both sides by converging reverse faults.

The fold is also affected by a network of small-offset faults of diverse kinematics. Reverse faults are the oldest and have recorded shortening perpendicular and parallel to the fold hinge. Strike-slip faults dominate with respect to the reverse faults, and developed mainly during the later stages of the fold evolution in the uppermost folded strata. Palaeostress tensors reconstructed by processing data of slickenside fault planes, indicate a NE-SW trending σ_1 that accompanied the earlier development of the fold, and a NW-SE trending σ_1, parallel to the fold hinge. A more recent NNE-SSW directed σ_1 is consistent with the Quaternary tectonic stress field of the region. Finally, extensional fractures developed in the later stage of fold evolution especially along the forelimb, due to local $\sigma_1 - \sigma_2$ substitution.

Acknowledgments

This study has been carried out in the framework of the NATO project SfP G4934 “Georgia Hydropower Security”, of the International Lithosphere Program - Task Force II, and of the European Space Agency project n. 32309 “Active tectonics and seismic hazard of southwest Caucasus by remotely-sensed and seismological data”. Seismic sections were kindly made available by the State Agency for Regulation of Oil and Gas Resources of Georgia (SAROGR). The authors acknowledge the use of the Move Software Suite granted by Midland Valley's Academic Software Initiative.

References

Adamia, Sh., Lordkipanidze, M.B., Zakariadze, G.S., 1977. Evolution of an active continental margins exemplified by the alpine history of the Caucasus. Tectonophysics 40, 183–199.
Adamia, Sh., Alania, V., Chabukiani, A., Chichua, G., Enukidze, O., Sadradze, N., 2010. Evolution of the Late Cenozoic basins of Georgia (SW Caucasus): a review. In: Sosson, M., Kaymakçı, N., Stephenson, R., Bergerat, F. (Eds.), Sedimentary Basin Tectonics From the Black Sea and Caucasus to the Arabian Platform. Geological Society of London, Special Publication 340, pp. 239–259.
Adamia, Sh., Alania, V., Chagelishvili, R., Chabukiani, A., Enukidze, O., Jaoshvili, G., Razmadze, A., Sadradze, N., 2011a. Tectonic setting of Georgia (Caucasus). 3rd International Symposium on the Geology of the Black Sea Region 1–10 October 2011, Bucharest, Romania. Abstracts Supplement to GEO-ECO-MARINA 17, pp. 11–13.
Adamia, Sh., Zakariadze, G., Chkhotua, T., Chabukiani, A., Sadradze, N., Tsereteli, N., Gventsadze, A., 2011b. Geology of the Caucasus: a review. Turk. J. Earth Sci. 20, 489–544.
Adamia, Sh., Alania, V., Tsereteli, N., Varazanashvili, O., Sadradze, N., Lursmanashvili, N., Gventsadze, A., 2017. Postcollisional tectonics and seismicity of Georgia. Geol. Soc. Am. Spec. Pap. 525, SPE525–17.
Alania, V., Chabukiani, A., Chagelishvili, R., Enukidze, O., Gogrichiani, K., Razmadze, A., Tsereteli, N., 2016. Growth structures, piggyback basins and growth strata of Georgian part of Kura foreland fold and thrust belt: implication for Late Alpine kinematic evolution. In: Sosson, M., Stephenson, R., Adamia, Sh. (Eds.), Tectonic Evolution of the Eastern Black Sea and Caucasus. Geological Society of London, Special Publications No. 428:p. 810 http://dx.doi.org/10.1144/SP428.5 (first published on October 27, 2015).
Angelier, J., 1990. Inversion of field data in fault tectonics to obtain the regional stress—III. A new rapid direct inversion method by analytical means. Geophys. J. Int. 103 (2), 363–376.
Apotria, T.G., 1995. Thrust sheet rotation and out-of-plane strains associated with oblique ramps: an example from the Wyoming salient USA. J. Struct. Geol. 17 (5), 647–662.
Apotria, T.G., Wilkerson, M.S., 2002. Seismic expression and kinematics of a fault-related fold termination: Rosario structure, Maracaibo Basin, Venezuela. J. Struct. Geol. 24 (4), 671–687.
Banks, C., Robinson, A., Williams, M., 1997. Structure and regional tectonics of the Achara-Trialeti fold belt and the adjacent Rioni and Kartli foreland basins. Republic of Georgia. In: Robinson, A.G. (Ed.), Regional and Petroleum Geology of the Black Sea and Surrounding Region. American Association of Petroleum Geologists Memoir No. 68, pp. 331–336.
Blaser, L., Krüger, F., Ohrnberger, M., Scherbaum, F., 2010. Scaling relations of earthquake source parameter estimates with special focus on subduction environment. Bull. Seismol. Soc. Am. 100 (6), 2914–2926.
Cardozo, N., Bhalla, K., Zehnder, A.T., Allmendinger, R.W., 2003. Mechanical models of fault propagation folds and comparison to the trishear kinematic model. J. Struct. Geol. 25 (1), 1–18.
Cavazza, W., Albino, I., Zattin, M., Galoyan, G., Imamverdiyev, N., Melkonyan, R., 2015. Thermochronometric evidence for Miocene tectonic reactivation of the Sevan–Akera suture zone (Lesser Caucasus): a far-field tectonic effect of the Arabia–Eurasia collision? In: Sosson, M., Stephenson, R.A., Adamia, S.A. (Eds.), Tectonic Evolution of the Eastern Black Sea and Caucasus. Geological Society, London, Special Publications:p. 428 http://dx.doi.org/10.1144/SP428.4
Chen, Y.-G., Lai, K.-Y., Lee, Y.-H., Suppe, J., Chen, W.-S., Lin, Y.-N.N., Wang, Y., Hung, J.-H., Kuo, Y.-T., 2007. Coseismic fold scarps and their kinematic behavior in the 1999 Chi-Chi earthquake Taiwan. J. Geophys. Res. 112, B03S02. http://dx.doi.org/10.1029/2006JB004388.
Costa, E., Vendeville, B.C., 2002. Experimental insights on the geometry and kinematics of fold-and-thrust belts above weak, viscous evaporitic décollement. J. Struct. Geol. 24 (11), 1729–1739.
Cowgill, E., Forte, A.M., Niemi, N., Avdeev, B., Tye, A., Trexler, C., Javakhishvili, Z., Elashvili, M., Godoladze, T., 2016. Relict basin closure and crustal shortening budgets during continental collision: an example from Caucasus sediment provenance. Tectonics 35 (12):2918–2947. http://dx.doi.org/10.1002/2016TC004295.
Dadiani, N., 1962. Life of Georgians (Tbilisi, 151 pages (in Georgian)).
Dubey, A.K., 1997. Simultaneous development of noncylindrical folds, frontal ramps, and transfer faults in a compressional regime: experimental investigations of Himalayan examples. Tectonics 16 (2), 336–346.
Dzhanelidze, A., Kandelaki, N., 1956. In: Kurochkin, V. (Ed.), Geological Map of the USSR, Caucasus Series Sheet K-38-XIII, Scale 1:200 000. Ministry of Geology and Mineral Protection USSR, Moscow.
Fiorini, E., Tibaldi, A., 2012. Quaternary tectonics in the central Interandean Valley, Ecuador: fault-propagation folds, transfer faults and the Cotopaxi Volcano. Glob. Planet. Chang. 90–91:87–103. http://dx.doi.org/10.1016/j.gloplacha.2011.06.002.
Fischer, M.P., Wilkerson, M.S., 2000. Predicting the orientation of joints from fold shape: results of pseudo–three-dimensional modeling and curvature analysis. Geology 28 (1), 15–18.
Fischer, M.P., Woodward, N.B., 1992. The geometric evolution of foreland thrust systems. Thrust Tectonics. Springer, Netherlands, pp. 181–189.
Fischer, M.P., Woodward, N.B., Mitchell, M.M., 1992. The kinematics of break-thrust folds. J. Struct. Geol. 14 (4), 451–460.
Forte, A., Cowgill, E., Bernardin, T., Kreylos, O., Hamann, B., 2010. Late Cenozoic deformation of Kura fold-thrust belt, southern Greater Caucasus. Geol. Soc. Am. Bull. 122, 465–486.
Forte, A., Cowgill, E., Whipple, K.X., 2014. Transition from a singly vergent to doubly vergent wedge in a young orogen: the Greater Caucasus. Tectonics 33, 2077–2101.
Homza, T.X., Wallace, W.K., 1995. Geometric and kinematic models for detachment folds with fixed and variable detachment depths. J. Struct. Geol. 17 (4), 575–588.

Jackson, J., Norris, R., Youngson, J., 1996. The structural evolution of active fault and fold systems in central Otago, New Zealand: evidence revealed by drainage patterns. J. Struct. Geol. 18 (2–3), 217–234.
Jamison, W.R., 1987. Geometric analysis of fold development in overthrust terranes. J. Struct. Geol. 9 (2), 207–219.
Koçyiğit, A., Yılmaz, A., Adamia, S., Kuloshvili, S., 2001. Neotectonics of East Anatolia Plateau (Turkey) and Lesser Caucasus: implication for transition from thrusting to strike-slip faulting. Geodin. Acta 14, 177–195.
Koronovskii, N.V., Demia, L.I., 1999. Collision stage of the evolution of the Caucasian sector of the Alpine fold belt: geodynamics and magmatism. Geotectonics 33, 102–118.
Lanza, F., Tibaldi, A., Bonali, F.L., Corazzato, C., 2013. Space–time variations of stresses in the Miocene–Quaternary along the Calama–Olacapato–El Toro Fault Zone, Central Andes. Tectonophysics 593, 33–56.
Li, Y., Jia, D., Shaw, J.H., Hubbard, J., Lin, A., Wang, M., Luo, L., Li, H., Wu, L., 2010. Structural interpretation of the coseismic faults of the Wenchuan earthquake: three-dimensional modeling of the Longmen Shan fold-and-thrust belt. J. Geophys. Res. 115, B04317.
Meijers, M.J., Smith, B., Pastor-Galán, D., Degenaar, R., Sadradze, N., Adamia, S., ... Langereis, C.G., 2015. Progressive orocline formation in the Eastern Pontides-Lesser Caucasus. Geol. Soc. Lond., Spec. Publ. 428, SP428–8.
Mitra, S., 1990. Fault-propagation folds: geometry and kinematic evolution, and hydrocarbon traps. AAPG Bull. 74, 921–945.
Mitra, S., 2003. A unified kinematic model for the evolution of detachment folds. J. Struct. Geol. 25 (10), 1659–1673.
Molinaro, M., Leturmy, P., Guezou, J.C., Frizon de Lamotte, D., Eshraghi, S.A., 2005. The structure and kinematics of the southeastern Zagros fold-thrust belt, Iran: from thin-skinned to thick-skinned tectonics. Tectonics 24 (3).
Mosar, J., Kangarli, T., Bochud, M., Glasmacher, U.A., Rast, A., Brunet, M., Sosson, M., 2010. Cenozoic–recent tectonics and uplift in the Greater Caucasus: a perspective from Azerbaijan. In: Sosson, M., Kaymakçı, N., Stephenson, R., Bergerat, F. (Eds.), Sedimentary Basin Tectonics From the Black Sea and Caucasus to the Arabian Platform. Geological Society of London, Special Publication 340, pp. 261–279.
Pace, P., Calamita, F., 2015. Coalescence of fault-bend and fault-propagation folding in curved thrust systems: an insight from the Central Apennines, Italy. Terra Nova 27 (175–183), 2015.
Pasquarè, F.A., Tormey, D., Vezzoli, L., Okrostsvaridze, A., Tutberidze, B., 2011. Mitigating the consequences of extreme events on strategic facilities: evaluation of volcanic and seismic risk affecting the Caspian oil and gas pipelines in the Republic of Georgia. J. Environ. Manag. 92 (7), 1774–1782.
Rebai, S., Philip, H., Dorbath, L., Borissoff, B., Haessler, H., Cisternas, A., 1993. Active tectonics in the Lesser Caucasus: coexistence of compressive and extensional structures. Tectonics 12 (5), 1089–1114.
Reilinger, R.E., McClusky, S.C., Vernant, P., Lawrence, S., Ergintav, S., Cakmak, R., Ozener, H., Kadirov, F., Guliev, I., Stepanian, R., Nadariya, M., Hahubia, G., Mahmoud, S., Sakr, K., Arrajehi, A., Paradissis, D., Al-Aydrus, A., Prilepin, M., Guseva, T., Evren, E., Dmirotsa, A., Filikov, S.V., Gomez, F., Al-Ghazzi, R., Karam, G., 2006. GPS constraints on continental deformation in the Africa-Arabia-Eurasia continental collision zone and implications for the dynamics of plate interactions. J. Geophys. Res. 111 (B5). http://dx.doi.org/10.1029/2005JB004051.
Rolland, Y., 2017. Caucasus collisional history: review of data from East Anatolia to West Iran. Gondwana Res. 49, 130–146.
Rowan, M.G., Linares, R., 2000. Fold-evolution matrices and axial-surface analysis of fault-bend folds: application to the Medina Anticline, Eastern Cordillera, Colombia. AAPG Bull. 84 (6), 741–764.
Sahakyan, L., Bosch, D., Sosson, M., Avagyan, A., Galoyan, G., et al., 2016. Geochemistry of the Eocene magmatic rocks from the Lesser Caucasus area (Armenia): evidence of a subduction geodynamic environment. Geol. Soc. Lond., Spec. Publ. 428, SP428.12.
Saintot, A., Angelier, J., 2002. Tectonic paleostress fields and structural evolution of the NW-Caucasus fold-and-thrust belt from Late Cretaceous to Quaternary. Tectonophysics 357, 1–31.
Sasvári, Á., Baharev, A., 2014. SG2PS (Structural Geology to Postscript Converter)–A graphical solution for brittle structural data evaluation and paleostress calculation. Comput. Geosci. 66, 81–93.
Shaw, J.H., Hook, S.C., Suppe, J., 1994. Structural trend analysis by axial surface mapping. AAPG Bull. 78 (5), 700–721.
Sosson, M., Kaymakci, N., Stephenson, R., Bergerat, F., Starostenko, V., 2010a. Sedimentary basin tectonics from the Black Sea and Caucasus to the Arabian Platform: introduction. Geol. Soc. Lond., Spec. Publ. 340 (1), 1–10.
Sosson, M., Rolland, Y., Danelian, T., Muller, C., Melkonyan, R., Adamia, S., Kangarli, T., Avagyan, A., Galoyan, G., 2010b. Subductions, obduction and collision in the Lesser Caucasus (Armenia Azerbaijan, Georgia), new insights. In: Sosson, M., Kaymakci, N., Stephanson, R., Bergarat, F., Storatchenoko, V. (Eds.), Sedimentary Basin Tectonics From the Black Sea and Caucasus to the Arabian Platform. Geological Society of London Special Publication 340, pp. 329–352.
Sosson, M., Adamia, S.H., Muller, C., Sadradze, N., Rolland, Y., Alania, V., Enukidze, O., Hassig, M., 2013. From Greater to Lesser Caucasus: new insights from surface and subsurface data along a N-S trending transect (Georgia): thick-skin versus thin-skin tectonics. Darius News 3, 5–7.
Suppe, J., 1983. Geometry and kinematics of fault-bend folding. Am. J. Sci. 283 (7), 684–721.
Suppe, J., Medwedeff, D.A., 1990. Geometry and kinematics of fault-propagation folding. Eclogae Geol. Helv. 83 (3), 409–454.
Tadono, T., Ishida, H., Oda, F., Naito, S., Minakawa, K., Iwamoto, H., 2014. Precise global DEM generation by ALOS PRISM. ISPRS Ann. Photogramm. Remote Sens. Spat. Inf. Sci. 2 (4), 71.
Takaku, J., Tadono, T., Tsutsui, K., 2014. Generation of high resolution global DSM from ALOS PRISM. Int. Arch. Photogramm. Remote. Sens. Spat. Inf. Sci. 40 (4), 243.
Tan, O., Taymaz, T., 2006. Active tectonic of the Caucasus: earthquake source mechanisms and rupture histories obtained from inversion of teleseismic body waves. Geol. Soc. Am. Spec. Pap. 409, 531–578.
Tanner, D.C., Behrmann, J.H., Dresmann, H., 2003. Three-dimensional retro-deformation of the Lechtal nappe, Northern Calcareous Alps. J. Struct. Geol. 25 (5), 737–748.
Thorbjornsen, K.L., Dunne, W.M., 1997. Origin of a thrust-related fold: geometric vs kinematic tests. J. Struct. Geol. 19 (3), 303–319.
Tibaldi, A., Alania, V., Bonali, F.L., Enukidze, O., Tsereteli, N., Kvavadze, N., Varazanashvili, O., 2017. Active inversion tectonics, simple shear folding and back-thrusting at Rioni Basin, Georgia. J. Struct. Geol. 96, 35–53.
Tsereteli, N., Tibaldi, A., Alania, V., Gventsadse, A., Enukidze, O., Varazanashvili, O., Müller, B.I.R., 2016. Active tectonics of central-western Caucasus, Georgia. Tectonophysics 691, 328–344.
Varazanashvili, O., Tsereteli, N., Tsereteli, E., 2011. Historical Earthquakes in Georgia (up to 1900): Source Analysis and Catalogue Compilation. Monograph. M. Javakhishvili Tbilisi State University, Georgia.
Vezzoli, G., Garzanti, E., Vincent, S.J., Andò, S., Carter, A., Resentini, A., 2014. Tracking sediment provenance and erosional evolution of the western Greater Caucasus. Earth Surf. Process. Landf. 39 (8), 1101–1114.
Wells, D.L., Coppersmith, K.J., 1994. New empirical relationships among magnitude, rupture length, rupture width, rupture area, and surface displacement. Bull. Seismol. Soc. Am. 84 (4), 974–1002.
Wickham, J., 1995. Fault displacement-gradient folds and the structure at Lost Hills, California (USA). J. Struct. Geol. 17 (9), 1293–1302.
Wilkerson, M.S., Medwedeff, D.A., Marshak, S., 1991. Geometrical modeling of fault-related folds: a pseudo-three-dimensional approach. J. Struct. Geol. 13 (7), 801–812.
Wilkerson, M.S., Apotria, T., Farid, T., 2002. Interpreting the geologic map expression of contractional fault-related fold terminations: lateral/oblique ramps versus displacement gradients. J. Struct. Geol. 24 (4), 593–607.
Williams, G., Chapman, T., 1983. Strains developed in the hangingwalls of thrusts due to their slip/propagation rate: a dislocation model. J. Struct. Geol. 5, 563–571.
Zakaraia, P., 1956. Architectural Complex of Tsaishi. Khelovneba Publ. House, Tbilisi (in Georgian).
Zanchi, A., Salvi, F., Zanchetta, S., Sterlacchini, S., Guerra, G., 2009. 3D reconstruction of complex geological bodies: examples from the Alps. Comput. Geosci. 35 (1), 49–69.
Zare, M., Amini, H., Yazdi, P., Sesetyan, K., Demircioglu, M.B., Kalafat, D., Erdik, M., Giardini, D., Khan, M.A., Tsereteli, N., 2014. Recent developments of the Middle East catalog. J. Seismol. 18 (4), 749–772.